BNL-101879-2014-TECH
AD/RHIC/RD/96;BNL-101879-2013-IR

RHIC Beam Tube-to-Flange Weld Evaluation

S. Kane

October 1995

Collider Accelerator Department
Brookhaven National Laboratory

U.S. Department of Energy
USDOE Office of Science (SC)

DISCLAIMER

AD/RHIC/RD–96

RHIC PROJECT

Brookhaven National Laboratory

RHIC Beam Tube-to-Flange Weld Evaluation

S. Kane, A. Farland, R. Sabatini, K. Warburton

October 1995

RHIC Beam Tube-to-Flange Weld Evaluation

S. Kane, A. Farland, R. Sabatini, K. Warburton

Abstract

Leaks and questionable penetration were found in some autogenous machine welded joints between the RHIC beam tube and flange located in the interconnect region. This investigation found the leaks were caused by hot cracking resulting from complications in welding low-sulfur, low-ferrite stainless steel. The marginal penetration is attributed to the joint design and the low sulfur content of the beam tube. Both problems are corrected using the same welding machine with specific electrode placement relative to the joint, and the addition of hydrogen to the shield gas. Repairs only should be accomplished with the addition of filler metal.

Background

After autogenously welding flanges to RHIC beam tubes using both automatic machine and manual welding, several leaks were detected in the weld. The flanges are American Iron and Steel Institute (AISI) Type 304 stainless steel with a 2.875 inch inside diameter and a 3.041 inch diameter counterbore into which the beam tube is inserted. The RHIC beam tube is a seamless, low-sulfur AISI Type 316LN, 2.875 inch diameter tube, 0.077 inch thick. The joint design calls for an autogenous square butt weld. The flanges are first tack welded to the tube in three places. Automatic machine welding was being performed using an Arc Machines, Incorporated (AMI) Model 207 power supply with an AMI custom welding head specifically designed for welding flanges to tube and pipe. Vacuum leak checking was then performed, resulting in detection of leaks in six automatic machine welds.

Automatic machine welded specimens were sectioned by manufacturing personnel to reveal a weld penetration of just 0.025 inch. Fit-up problems also were detected. These are categorized as beam tube ovality, beam tube not square, and flange counterbore root radius. Beam tubes may be out-of-round by 0.030 inch for raw stock, and have been found out-of-round by as much as 0.100 inch after welding to the end volume. This appears to affect the fit of the Wachs tube cutter. The cutter is capable of making cuts square within 0.002 inch per inch of tube diameter. However, beam tube ends have been found to be as much as 0.019 inch out-of-square. Finally, the flanges have different radii at the root of the counterbore. The large radius prevents the tube from contacting the flange shoulder, creating a gap at the weld joint.

An additional concern was the weld operator practice of wire brushing the weld after welding. A wire bristle within the beam tube would have undesirable consequences during Collider operation. Even though stainless steel brushes were used, the AISI Type 301 stainless steel bristles are

magnetic. Corrective actions to assure a clean beam tube were instituted, though unrelated to this investigation.

Initial corrective action was to discontinue automatic machine welding in favor of manual welding until this weld investigation is completed. Minimum required weld penetration is 0.025 inch. All beam tube flange welding will be by the automatic machine process upon successful completion of this investigation. Only small radius flanges would be used for future production, and large radius flanges would be re-machined to the smaller radius. Welds would be cleaned using alcohol only.

Procedure

The sample welds to be evaluated were made using short lengths of the actual beam tube and production flanges. The automatic welding machine used was a Dimetrics PTW-150 tube welder fitted with an AMI Model 09-2500 weld head especially modified to mount a flange on the head for tube-to-flange welding. The machine has a power supply with a 100 ampere continuous rated output at 100% duty cycle with 150 ampere peak pulsed capability, and includes a torch coolant system with a 2.3 liter reservoir and heat exchanger mounted within the cabinet.

The power supply is designed to produce continuous or pulsed current. The tube welding system has two closed-loop servos, permitting extremely accurate timing, speeds and pulse rates. One servo controls welding amperage and the other controls the motor speed in the tube weld head. The machine is capable of synchronized pulsing of all parameters with programmable frequency and pulse width, and programmable current sloping between segments. Voltage is automatically determined by the gap between the electrode and the work, the electrode geometry, and the shield gas. Bead width and penetration are controlled by primary and background current settings, pulse width, pulse spacing, and travel speed.

The machine has internal memory storage for 16 different welding programs containing up to 16 segments in each program, and comes with computer-originated welding schedules developed for welding thin-wall, 300 series stainless steel alloy tubing. These welding schedules are based upon calculations which may have ranging results due to factors such as:

- variations in tube diameter and wall thickness,
- variations in the specific heat of the tube alloy,
- variations in surface condition, and
- speed calibration of the weld head used.

Initial values are on the "cool" side to prevent burn-through. To produce perfect welds, the machine has a current "Scale Factor" function to increase or decrease the heat input.

The weld head has a "home" position for the electrode, between the 1:00 o'clock and 2:00 o'clock position, from which the weld program begins. The weld program begins with a pre-purge flow of shield gas. Once the arc is initiated, the power supply begins the first segment, moving the rotor to the 1:00 o'clock position to begin welding. This is performed at low current

and maximum travel speed. Segment 2 is a Pre-heat and Pause. The electrode is paused while current is increased to achieve full penetration. Segments 3 through 6 are divided into four equally timed periods during which the weld head will rotate the electrode completely around the tube in a counter-clockwise direction, as viewed from the flange-side of the joint. Primary current is reduced during subsequent segments because less current is needed for maximum weld penetration as the heat builds up in the weldment. The power supply enters a down slope phase to taper off the weld after segment 6 is completed, then activates a post-purge timer.

Initial production welding was performed using 99.999% pure, laboratory grade argon as a shield gas, which is the standard practice at Brookhaven National Laboratory. Other investigation found significant advantages to using a shield gas mixture of 95% argon and 5% hydrogen. Both gases would be used for this investigation.

Repeatability in the welding procedure depends significantly upon the electrode gap and geometry. A 3/32 inch diameter, ground-finish, 2% thoriated tungsten electrode was prepared with a ground point angle of 60° and a 0.020 inch diameter flat ground on the point. The electrode-to-work distance was set at 0.060 inch because of the ovality of the tubes. The test specimens were welded with different axial electrode locations indexed from the seam. Electrode locations used in this investigation were 0.010 inch toward the flange side of the seam, right on the seam, and 0.016 inch toward the tube, and is shown in the work sheets (Appendix A). The flange and beam tube inside diameters varied 0.002 inch. Average radial clearance between the beam tube and flange was 0.017 inch. The flanges were seated against the tube end with no end gap and off center, with the flange pushed radially to one side, such that the tube side would be touching the flange on one side with a maximum possible gap on the opposite side of the circumference. The flange was then tack welded to the beam tubes in three places to maintain gap-free fit-up during welding.

Ten sample welds were prepared using various weld schedules. The weld schedules are shown in Table 1. After these initial sample welds were sectioned and examined, the two schedules producing the best penetration were retested, this time with the orientation of the specimens marked in order to evaluate what effect gravity might have upon weld penetration. The sample welds were sectioned using traveling wire electro-discharge machining at the point of closest and greatest radial clearance between the pipe and the flange.

Each specimen was ground by hand on silicon carbide papers, beginning with 240 grit, followed by 320 grit, 400 grit, and ending with 600 grit. A mixture of kerosene and paraffin was used as a lubricant. The specimens were cleaned with ethanol in an ultrasonic cleaner after each step. The specimens were then polished in two steps using a 6μ diamond paste followed by a 1μ diamond paste. Both steps were performed using a nylon cloth on a 203mm rotating wheel with Buehler's metadi fluid — a solution of water and polypropylene glycol — as a lubricant. Again, the specimens were cleaned with ethanol in an ultrasonic cleaner after each step. Finally, the specimens were electrolytically etched using a 10% solution of oxalic acid and distilled water and a stainless steel cathode. A ten volt electrical potential was applied for approximately 15 seconds.

Table 1
Weld Schedules

Weld Schedule	Weld Parameters	Segment Number					
		1	2	3	4	5	6
1	Duration (sec)	7	2	24	24	24	24
	Current (amp)	13	84.5	84.5	83.2	81.9	80.6
2	Duration (sec)	7	2	26	26	26	26
	Current (amp)	23	94.5	94.5	93.2	91.9	90.6
3	Duration (sec)	7	2	26	26	26	26
	Current (amp)	23	114.5	114.5	113.2	111.9	110.6
4	Duration (sec)	7	2	26	26	26	26
	Current (amp)	23	124.5	124.5	123.2	121.9	120.6
5	Duration (sec)	7	2	26	26	26	26
	Current (amp)	23	144.5	144.5	143.2	141.9	140.6

The specimens were examined using a Reichert-Jung Model MeF3 inverted stage metallograph equipped with a 100 watt low voltage halogen bulb. Photographs were taken on Polaroid 553, 4 inch x 5 inch, coaterless medium-contrast instant film using a Reichert-Jung Type 6532-01 Exposure Control. Specimens were photographed at 25x, then the weld dimensions were taken from the photograph using a 0.001 inch graduation scale also photographed at 25x. Specimen #12A was photographed at 20x because the weld was too wide to fit within the camera frame at 25x. The leaking weld specimen also was examined using secondary electron emissions on a JEOL Model JSM-6400 Scanning Electron Microscope with an incident beam energy of 5 kV.

Results and Discussion

Penetration

The test weld dimensions are detailed in Table 2, and the metallographs are shown in Figures 1 through 24. All test welds achieved the minimum required penetration of 0.025 inch. However, the welds using 5% hydrogen achieved greater penetration with 21% less heat input than the welds using 100% argon. Figure 27 shows the average weld penetration measured at the seam versus the primary welding current. The data are categorized by the shield gas and electrode location. This is annotated in the legend by the distance, in inches, and the direction of displacement (toward the **flange**, directly over the **seam**, or toward the **tube**). The penetration in the tube was greater than the penetration at the seam or in the flange where the heat input was greater — as the electrode location was toward the tube, at higher heat inputs, and where the radial clearance was greatest. Greater penetration in the tube alone is not desirable, and resulted in leaks in the weld where the electrode was located 0.016 inch from the seam toward the tube. This was examined in a scanning electron microscope at 170x and 500x, shown in Figures 25 and 26, respectively.

Table 2
Test Weld Dimensions

Weld Number	Weld Schedule	Shield Gas	Electrode Location	Penetration			Bead Width		End Gap	Side Gap	Comments
				Seam	Tube	Flange	Flange	Tube			
1A	1	95Ar/5H	0	0.026	0.037	0.027	0.072	0.106	0.003	0.013	Favors tube
1B	1	95Ar/5H	0	0.030	0.030	0.030	0.079	0.090	0	0	
2A	2	95Ar/5H	0	0.025	0.033	0.027	0.076	0.114	0.002	0.004	Slight favor of tube
2B	2	95Ar/5H	0	0.026	0.039	0.029	0.082	0.114	0.003	0.012	Favors tube
3A	2	95Ar/5H	0.010" F	0.026	0.026	0.025	0.086	0.101	0.001	0.008	
3B	2	95Ar/5H	0.010" F	0.027	0.027	0.027	0.092	0.092	0	0.003	Even penetration
4A	1	95Ar/5H	0.010" F	0.028	0.028	0.027	0.089	0.081	0	0.015	Even penetration
4B	1	95Ar/5H	0.010" F	0.028	0.028	0.027	0.084	0.085	0	0	Even penetration
5A	3	95Ar/5H	0.010" F	0.033	0.039	0.033	0.095	0.104	0.001	0.008	
5B	3	95Ar/5H	0.010" F	0.032	0.032	0.031	0.095	0.096	0	0.001	Even penetration
6A	2	100Ar	0.010" F	0.026	0.032	0.025	0.076	0.079	0	0.012	
6B	2	100Ar	0.010" F	0.026	0.028	0.026	0.073	0.081	0	0.004	
7A	3	100Ar	0.010" F	0.028	0.031	0.028	0.076	0.080	0	0.001	
7B	3	100Ar	0.010" F	0.029	0.036	0.031	0.098	0.092	0.002	0.014	Notch at seam
8A	4	100Ar	0.010" F	0.029	0.044	0.032	0.096	0.108	0.002	0.019	Favors tube
8B	4	100Ar	0.010" F	0.020	0.025	0.020	0.099	0.093	0	0	
9A	4	100Ar	0.016" T	0.030	0.061	0.030	0.064	0.139	0.002	0.010	Heavy favor of tube
9B	4	100Ar	0.016" T	0.008	0.031	0.021	0.062	0.120	0.002	0.002	Voids in weld
10A	5	100Ar	0	0.028	0.052	0.029	0.105	0.131	0.002	0.008	Favors tube
10B	5	100Ar	0	0.032	0.033	0.032	0.106	0.124	0.002	0.001	
11A	2	95Ar/5H	0.010" F	0.030	0.033	0.030	0.100	0.090	0.002	0.020	
11B	2	95Ar/5H	0.010" F	0.027	0.027	0.026	0.095	0.083	0.001	0.006	Even penetration
12A	3	95Ar/5H	0.010" F	0.029	0.033	0.028	0.112	0.108	0.002	0.004	Even penetration
12B	3	95Ar/5H	0.010" F	0.034	0.042	0.033	0.112	0.098	0.002	0.027	

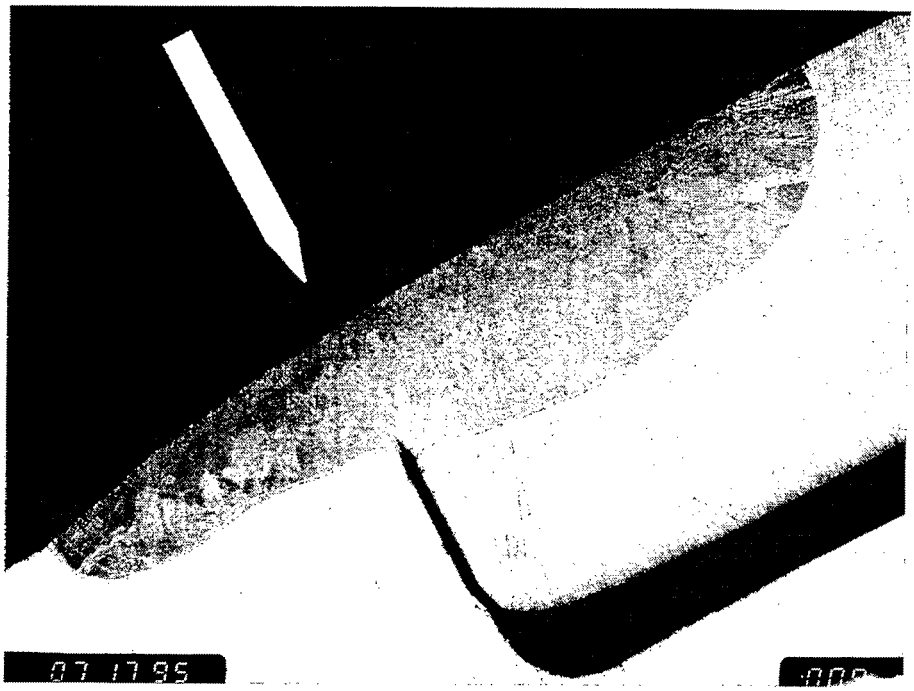

Figure 1 - Specimen 1A (25x)

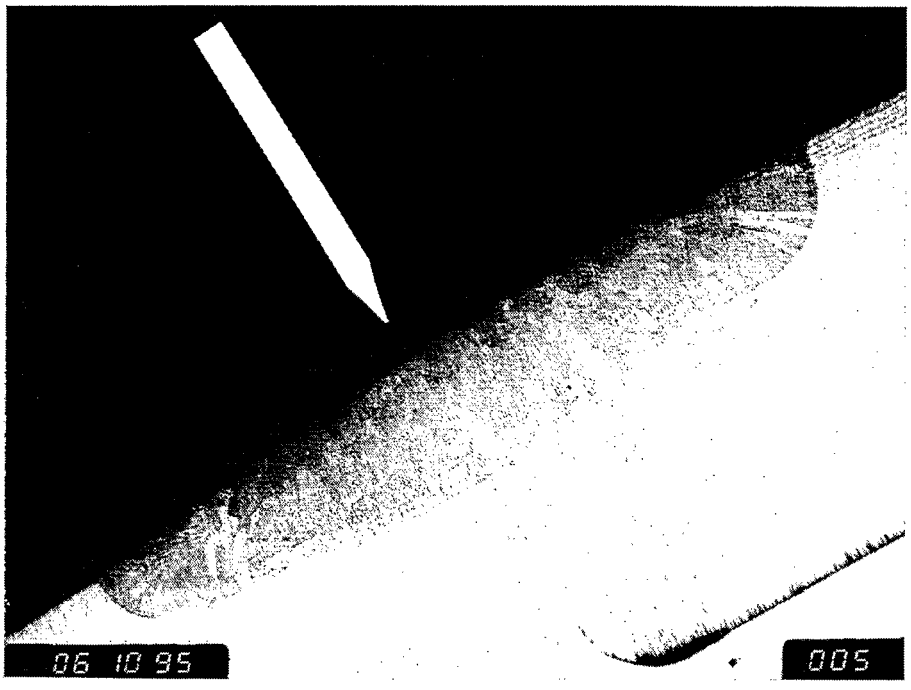

Figure 2 - Specimen 1B (25x)

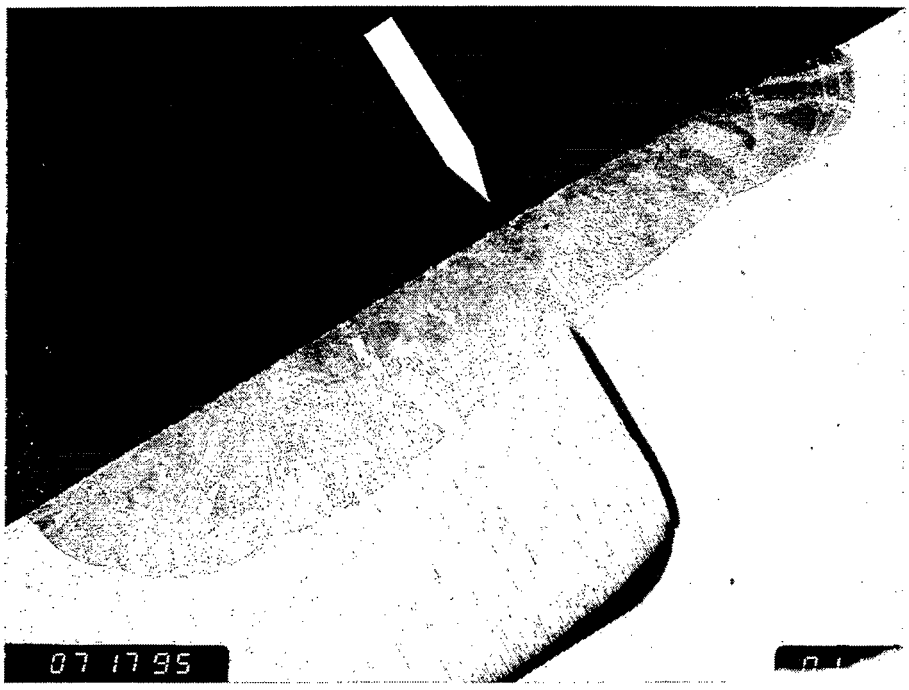

Figure 3 - Specimen 2A (25x)

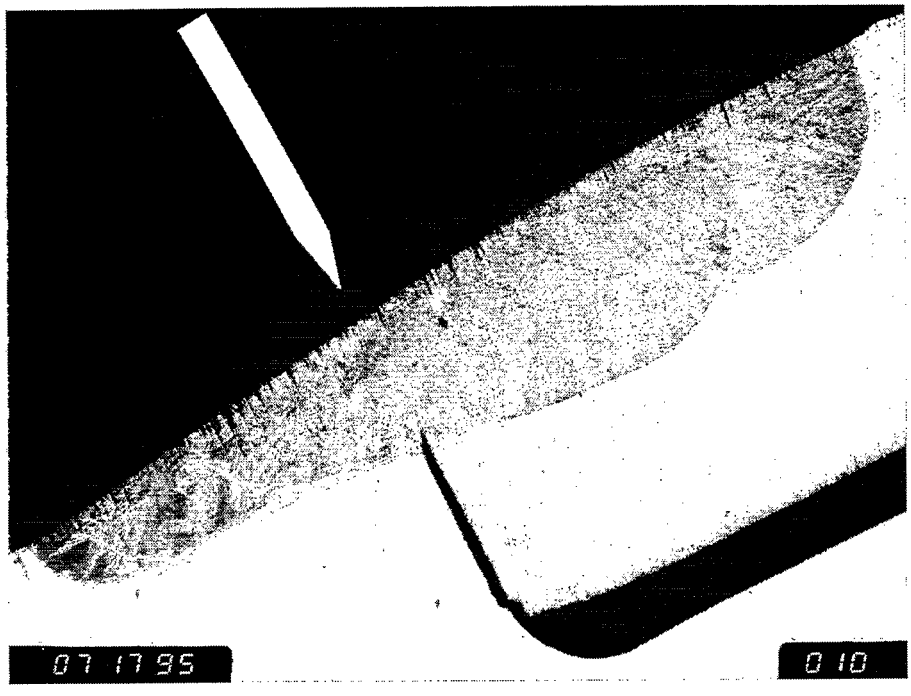

Figure 4 - Specimen 2B (25x)

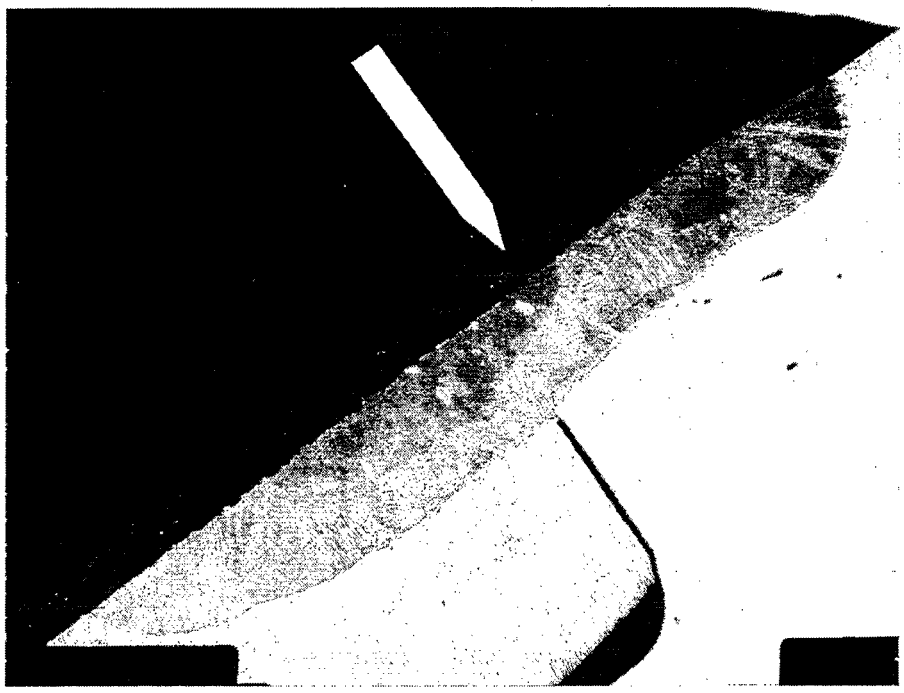

Figure 5 - Specimen 3A (25x)

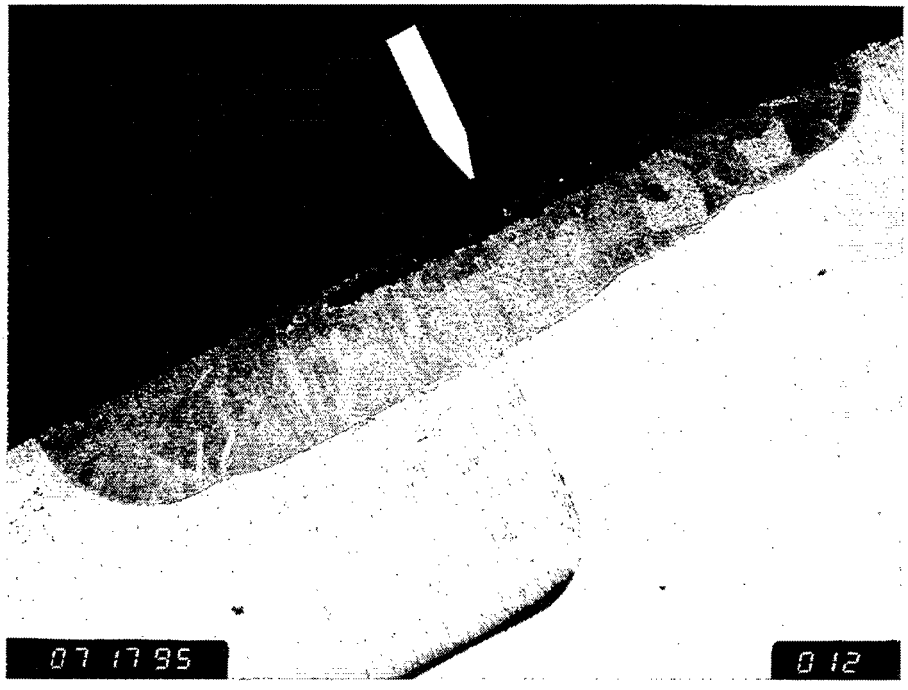

Figure 6 - Specimen 3B (25x)

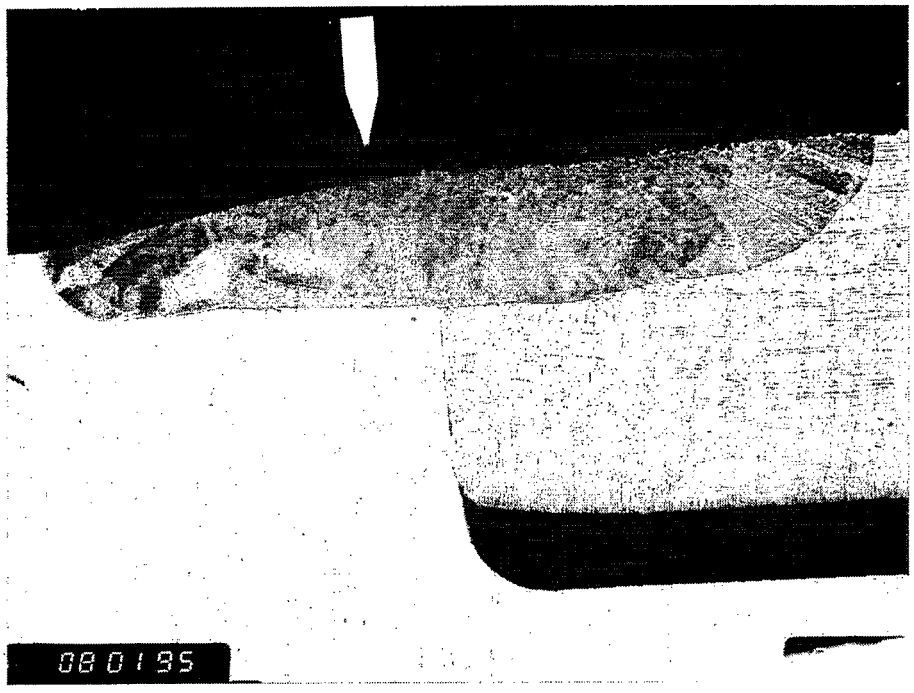

Figure 7 - Specimen 4A (25x)

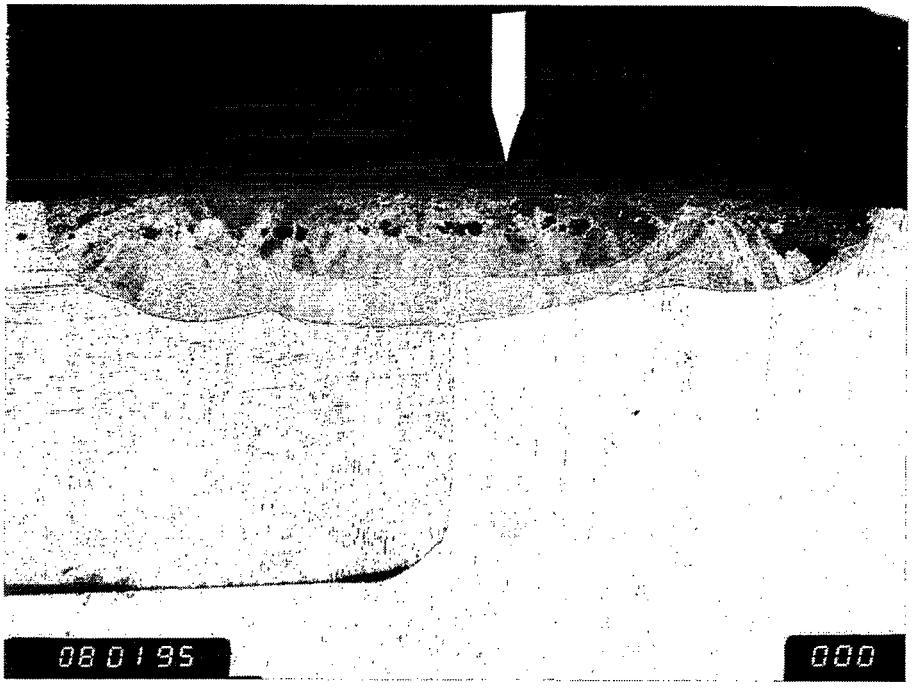

Figure 8 - Specimen 4B (25x)

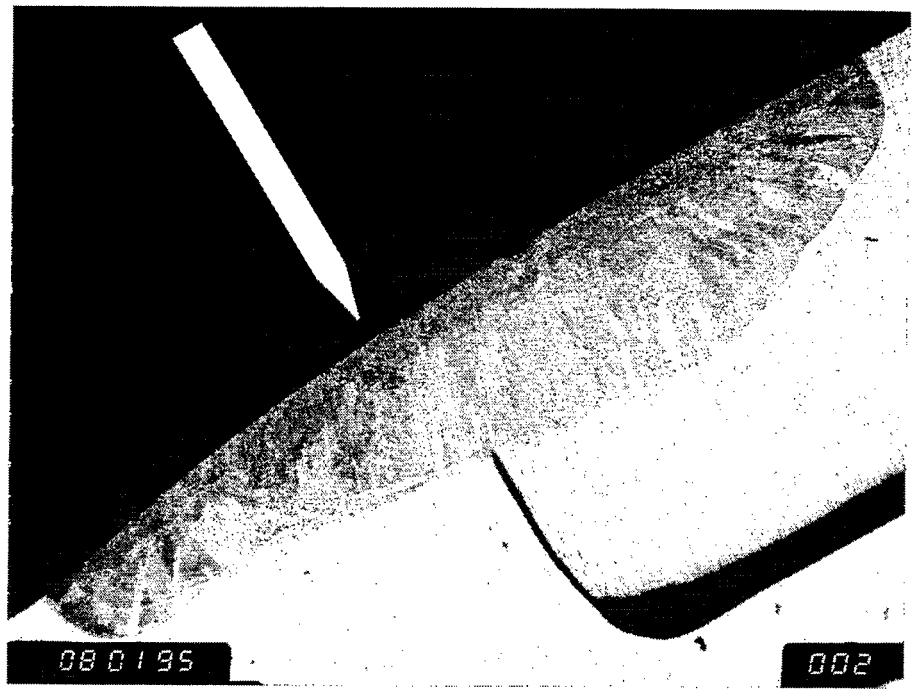

Figure 9 - Specimen 5A (25x)

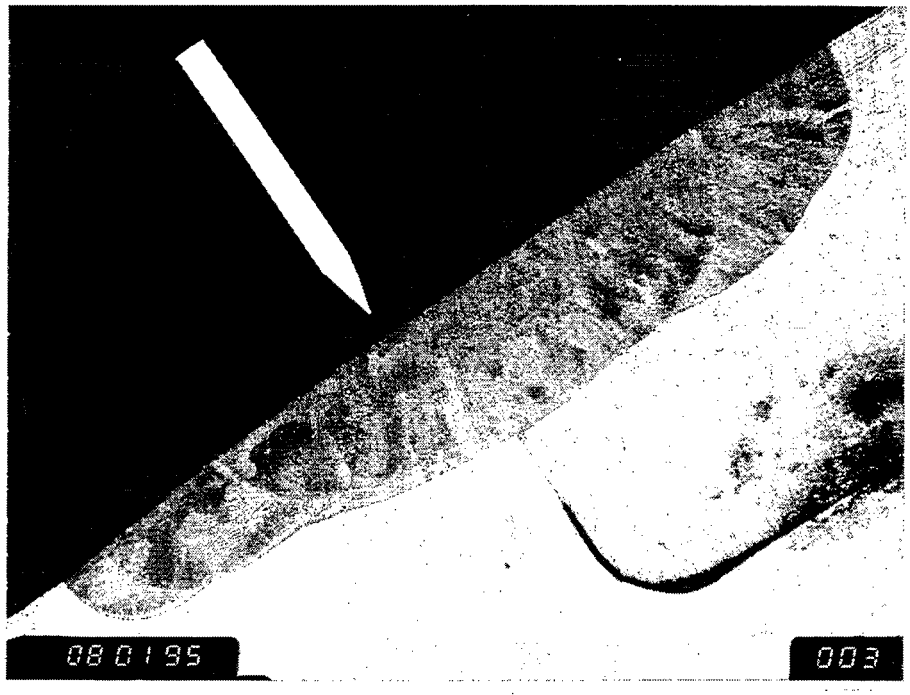

Figure 10 - Specimen 5B (25x)

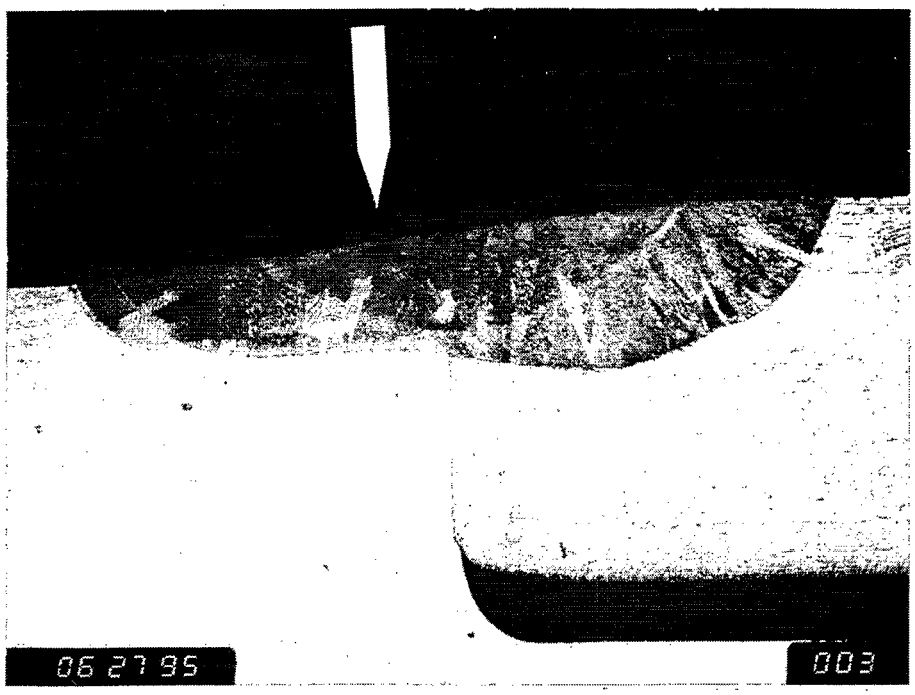

Figure 11 - Specimen 6A (25x)

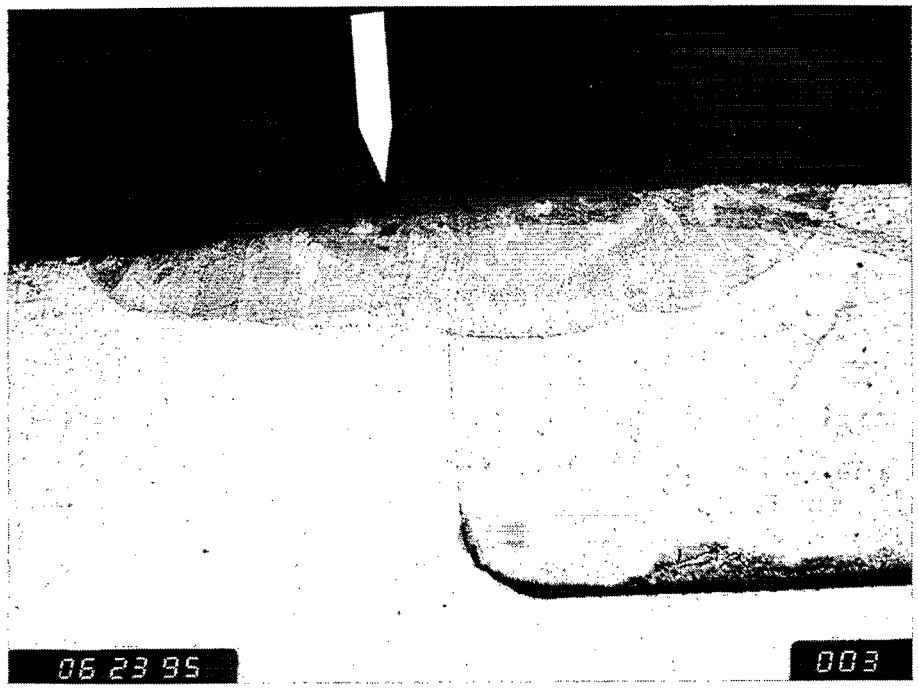

Figure 12 - Specimen 6B (25x)

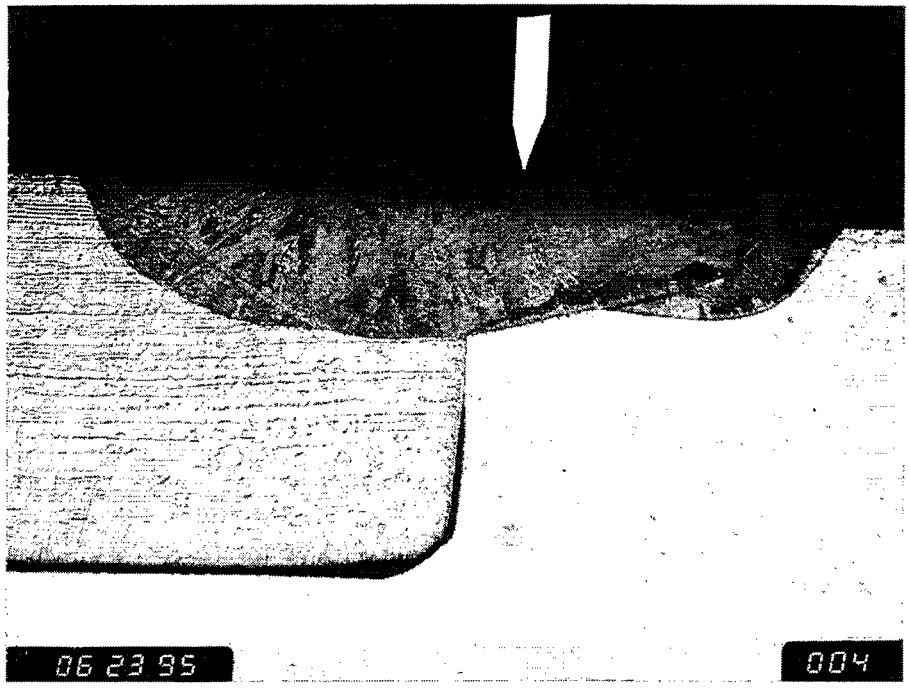

Figure 13 - Specimen 7A (25x)

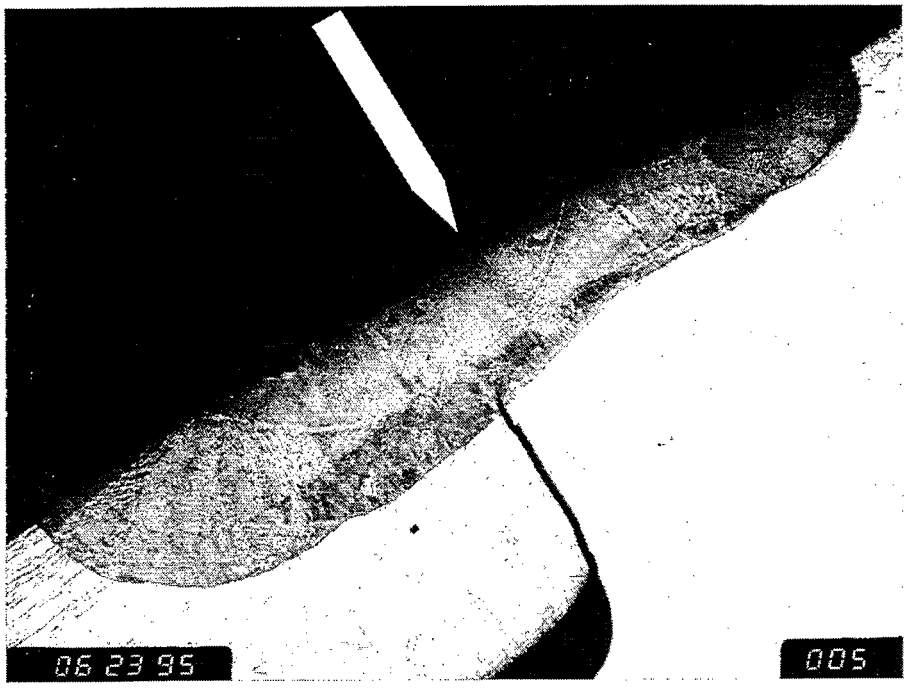

Figure 14 - Specimen 7B (25x)

Figure 15 - Specimen 8A (25x)

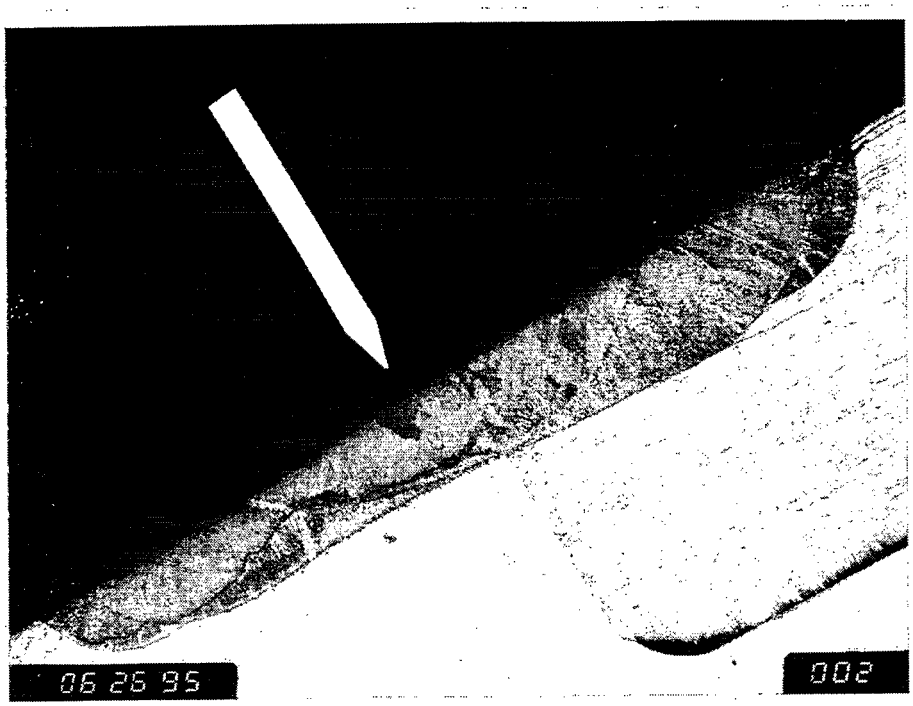

Figure 16 - Specimen 8B (25x)

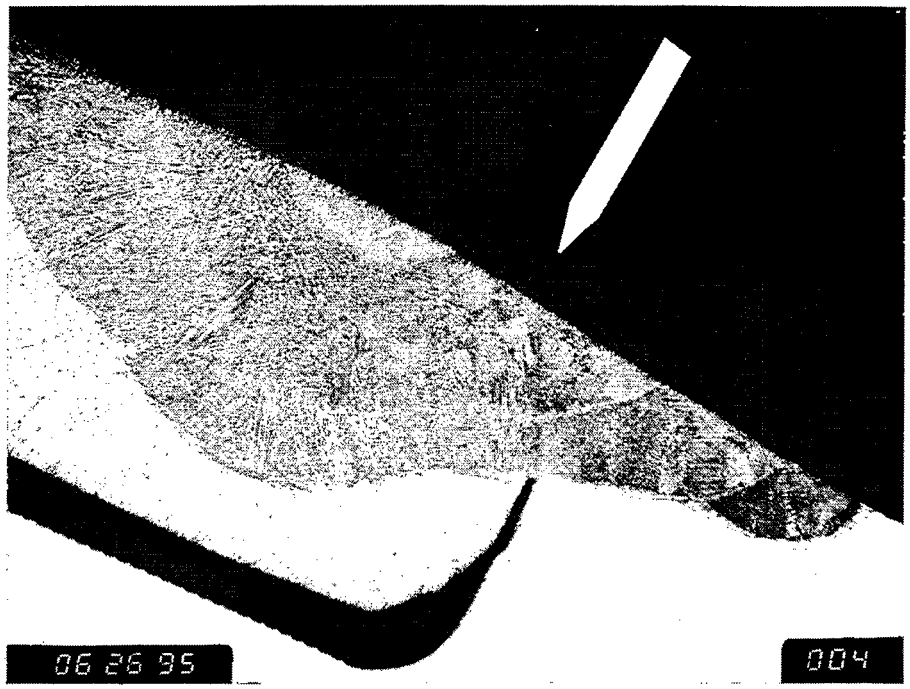

Figure 17 - Specimen 9A (25x)

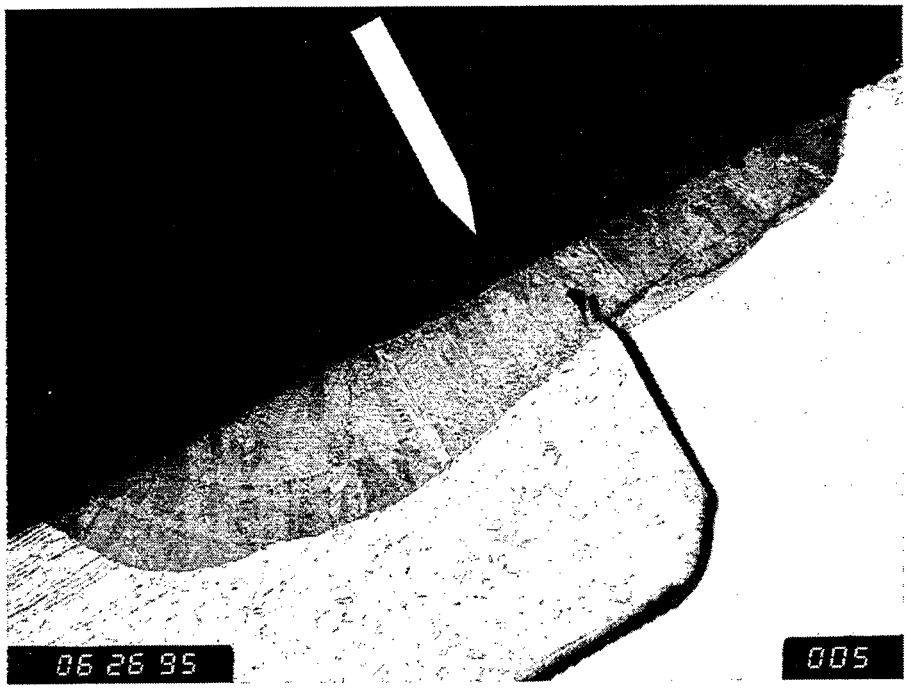

Figure 18 - Specimen 9B (25x)

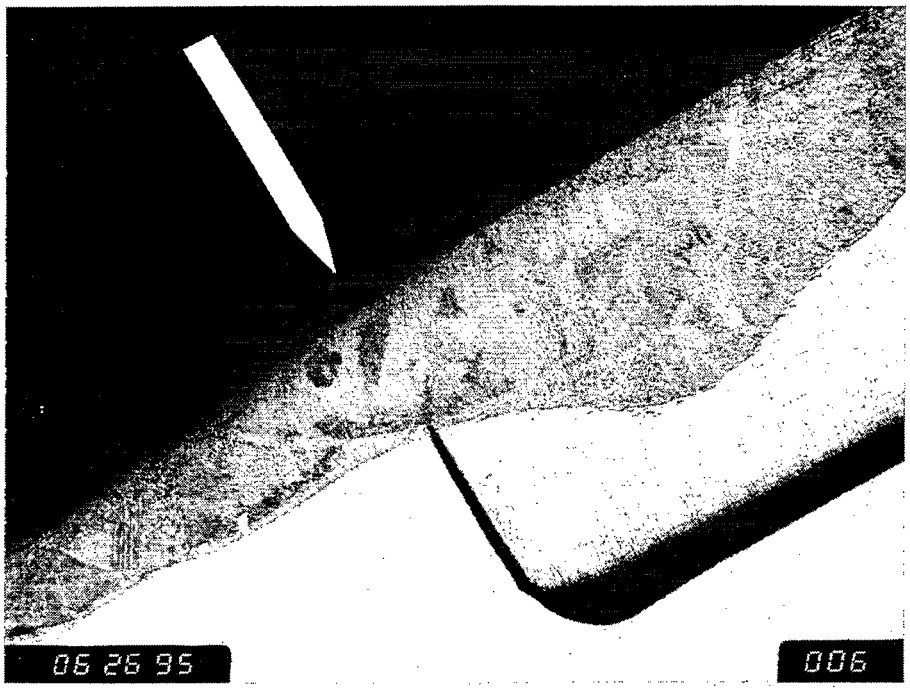

Figure 19 - Specimen 10A (25x)

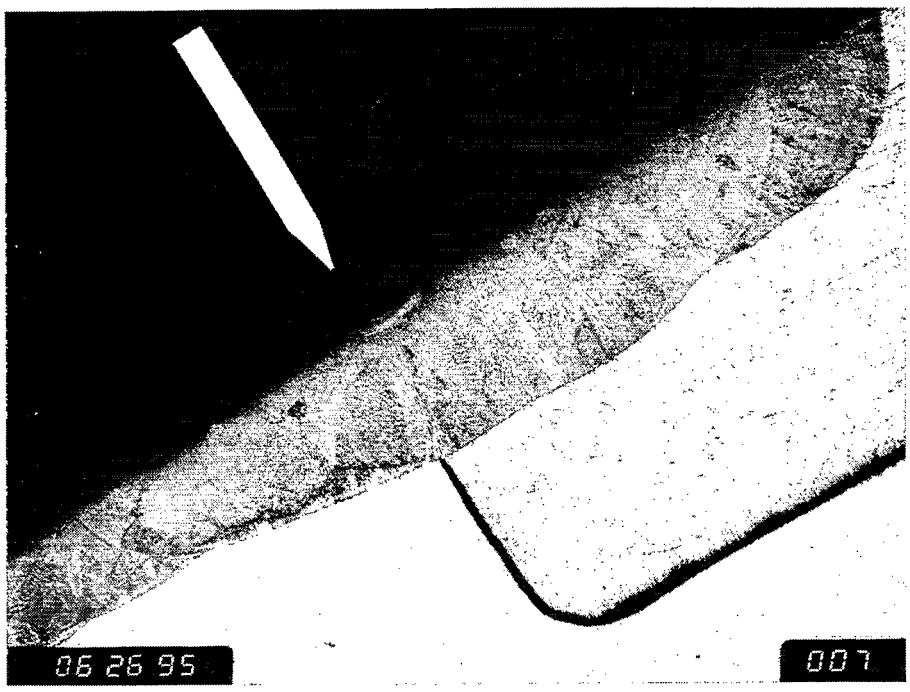

Figure 20 - Specimen 10B (25x)

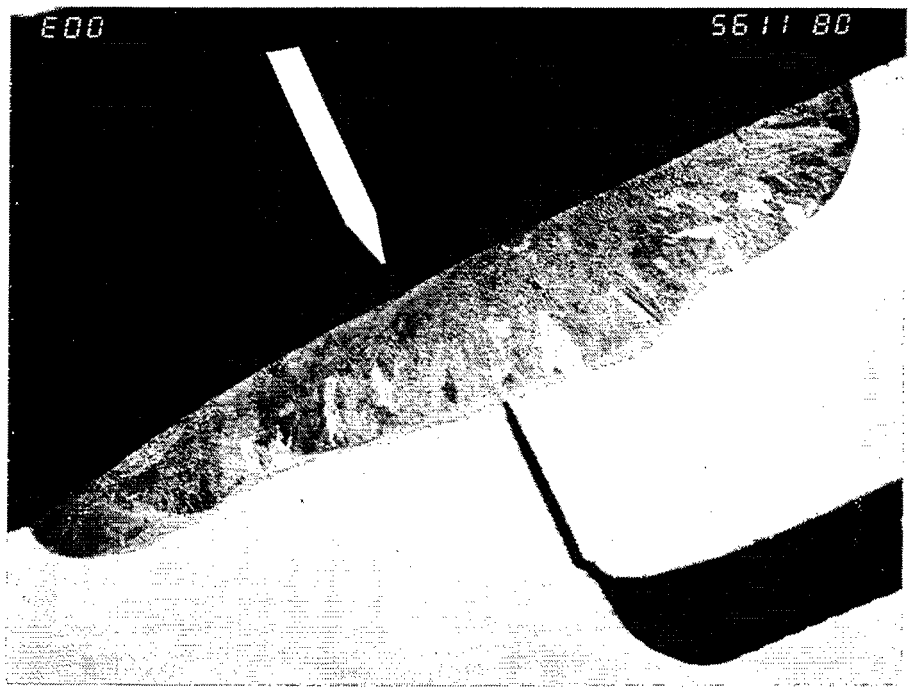

Figure 21 - Specimen 11A (25x)

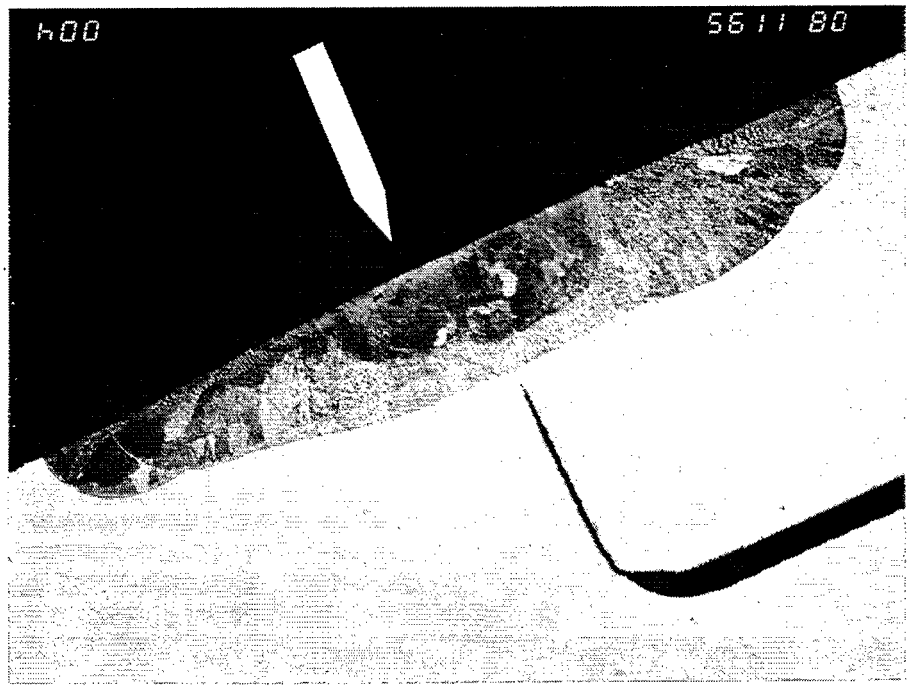

Figure 22 - Specimen 11B (25x)

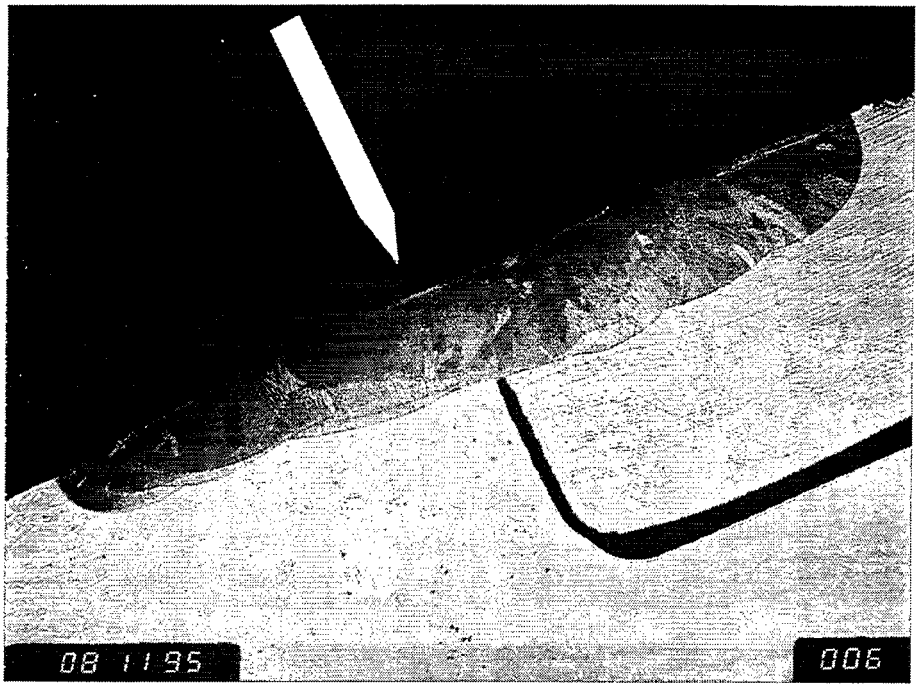

Figure 23 - Specimen 12A (20x)

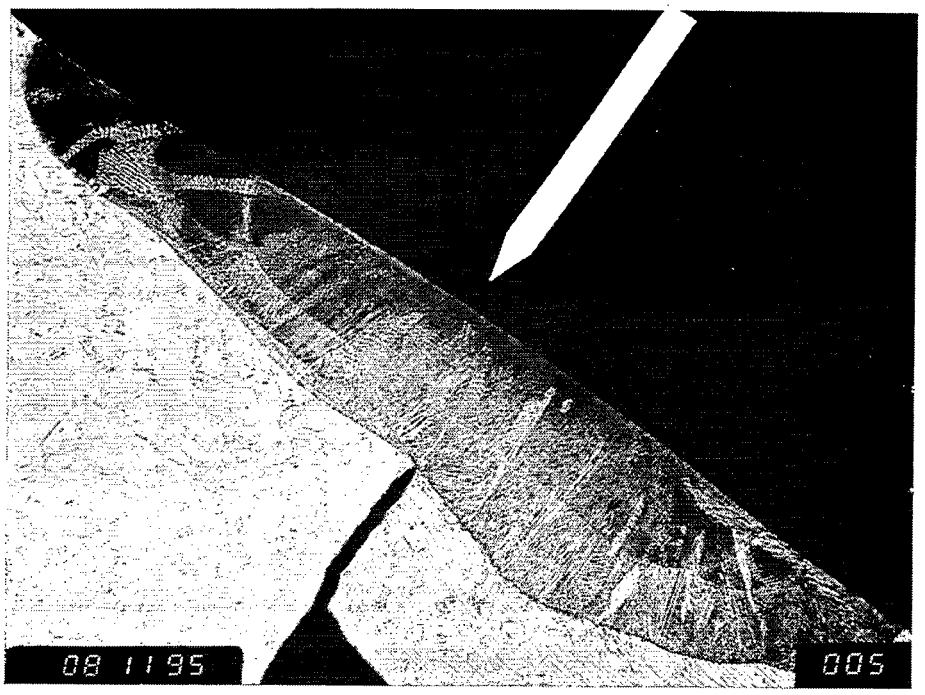

Figure 24 - Specimen 12B (25x)

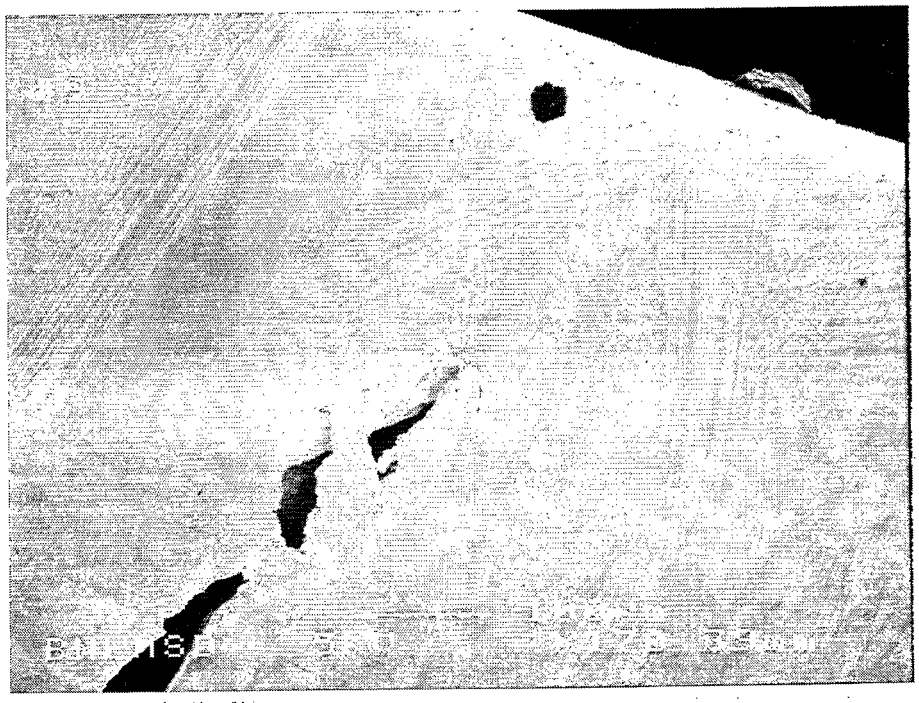

Figure 25 - Leaks in Specimen 9B (170x)

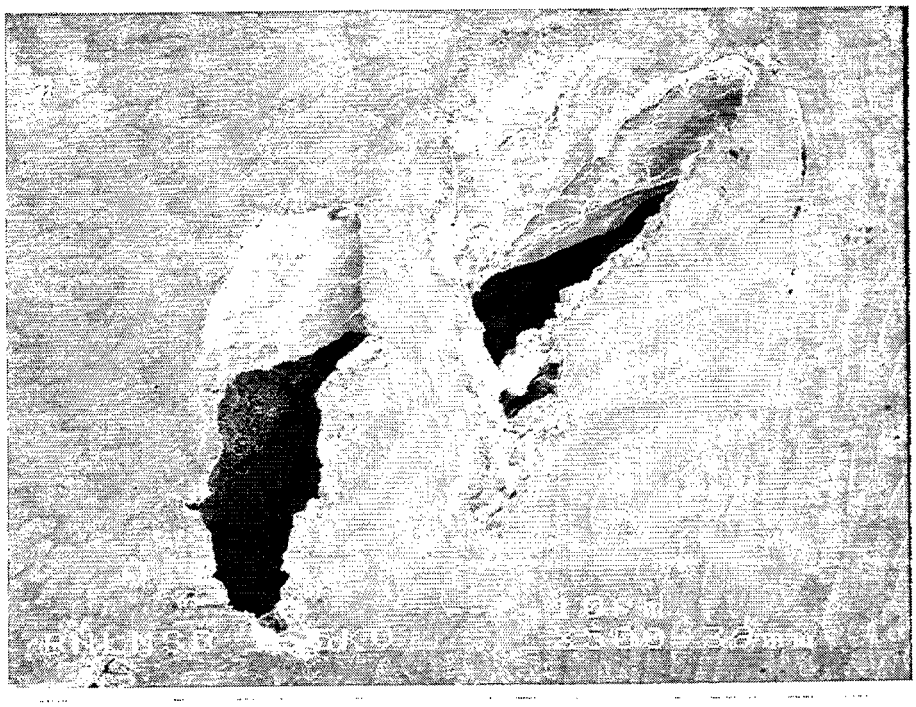

Figure 26 - Leaks in Specimen 9B (500x)

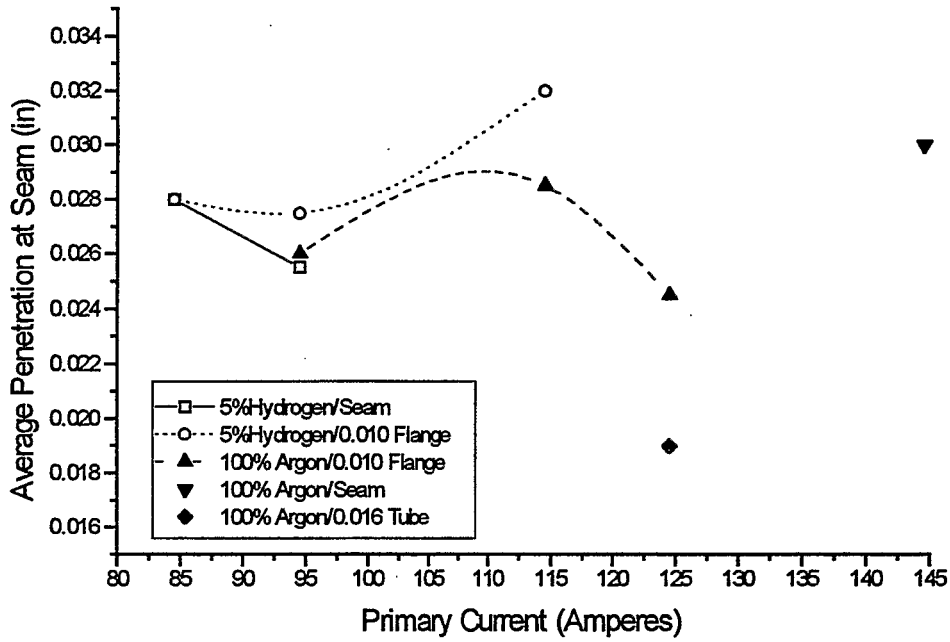

Figure 27 - Average Seam Penetration

Figure 28 shows the total weld width for the sample welds. The data are categorized by the shield gas and electrode location, just as in Figure 27. This figure shows the welds produced with the hydrogen added to the shield gas were wider than the welds produced without the hydrogen additions. The average width for the welds produced with the hydrogen added to the shield gas was 9% wider than the welds produced without the hydrogen additions. This result alone is not significant to the investigation for penetration, but when coupled with the greater penetration, the total volume of the welds produced with the hydrogen added to the shield gas is significantly larger. In this study, the volume of the welds produced with the hydrogen added to the shield gas was 21% greater than the welds produced without the hydrogen additions. The greater weld volume demonstrates the efficiency of the heat input when hydrogen is added to the shield gas. Finally, the side clearance was compared to the weld penetration. Specifically, the penetration depth for the high clearance specimens was compared with the penetration depth of the low or zero clearance specimens from the same sample weld. The results failed to show a relationship between side clearance and weld penetration, but this may be masked by variation in the electrode gap as the electrode rotates around the work.

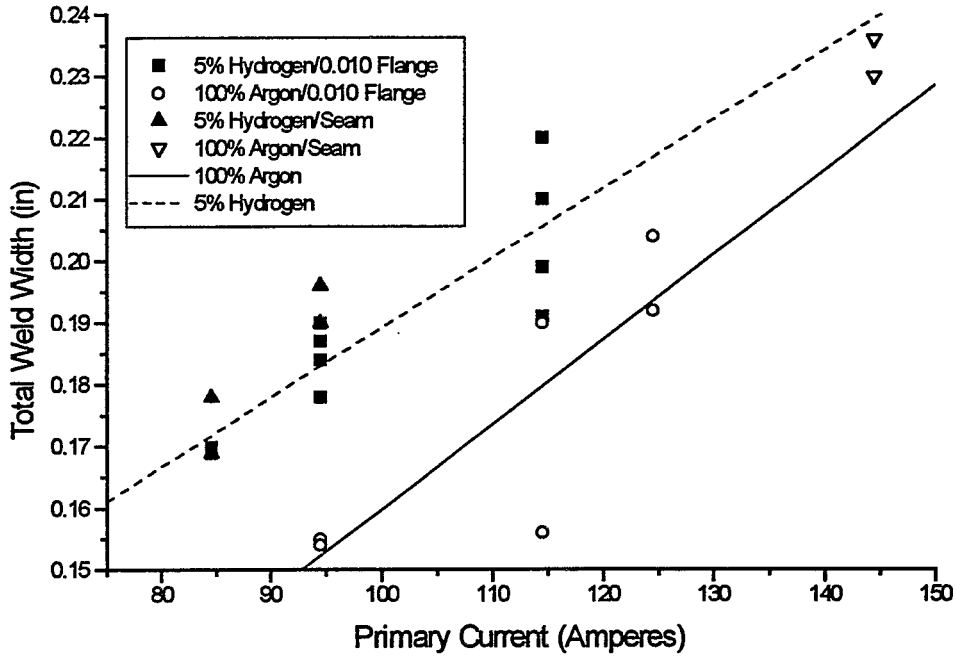

Figure 28 - Total Weld Width

Effects of Shield Gas

Welding gas composition plays an important role in the gas tungsten arc welding (GTAW) process, and good shield gas coverage is mandatory for low heat input welds. Nothing will cause more welding problems than improper or contaminated shield gas coverage. The electric arc is produced by the passage of current through the conductive, ionized shielding gas. Pure argon is the gas most often used. This gas is inert, safe, relatively inexpensive and very easily ionized. Argon may be mixed with hydrogen, helium or oxygen to produce a more intense arc.

Relevant properties of commonly used shield gases[1,2] are shown in Table 3. The numbers in parentheses represent the changes in the ionizing potential as the gas transitions through the metastable excited stages to the ionized state. Hydrogen and helium have eight to ten times the thermal conductivity of argon, thus significantly improving the uniformity of the thermal ionization across the plasma. A mixture of 75% helium and 25% argon is a standard, commercially-available mixture that can produce narrower, deeper welds at less current than pure argon. Helium, however, has a much higher ionizing potential, even in the ionized state, than argon or hydrogen, making arc starts more difficult. Frequently the ratio of helium and argon is reduced to 15% to achieve consistent low energy arc starts. If the arc start energy needed to ionize the welding gas is too high, a small overmelt or material expulsion at the start location will result. Helium cannot be used in any ultra high vacuum system welding for the RHIC Project, which includes the beam tube.

Small percentages of hydrogen in argon, between 2% to 5%, increases arc voltage, producing a hotter, more confined arc as does helium. In addition, hydrogen provides a reducing atmosphere

that tends to remove oxides in the weld area. This reducing effect also promotes metal flow through reduced puddle surface tension. This gas combination used with a high frequency pulsed arc produces the lowest heat input welds possible with the GTAW process. Hydrogen is not without its detractors. Higher concentrations of hydrogen may cause porosity in the weld, and may cause embrittlement and cracking in high strength carbon steels. The practice in the industry is to use up to 5% hydrogen with argon in the shield gas for greater penetration when welding thin stainless steel tube and sheet.

In this investigation we have found that the addition of hydrogen produce 14% greater penetration, all other parameters being equal. The welds produced with hydrogen additions were exceptionally oxidation-free, with little or no cleaning required. This contrasts with the high heat 100% argon welds which required wire brushing to remove the oxidation.

Table 3
Some Important Properties of Welding Shield Gases

Gas	Thermal Conductivity ($cal/cm^2/cm/sec/^oC \times 10^{-4}$)	Ionization Potential (eV)
Argon	0.4	15.760 (11.548)
Hydrogen	4.1	15.43
H_2		15.43
H		13.598
Helium	3.3	24.5876 (20.9643) (19.8198)

Effects of Sulfur

Sulfur has a unique and pronounced effect upon the molten weld pool and weld penetration. Sulfur has a positive surface tension coefficient which decreases the surface tension at the liquidus of iron. However, the surface tension increases as the temperature of the molten metal increases. This creates a higher surface tension in the center of the weld pool which draws the molten metal toward the center. This reverses the Marangoni convection pattern, thrusting the hotter metal at the center of the weld pool downward and increasing penetration[2]. Sulfur has a pronounced effect upon penetration and is sometimes specified as a minimum in steels intended for extensive automatic GTAW to guarantee consistent weld penetration.

A normal sulfur heat contains 0.008% to 0.030% and a low heat contains 0.001% to 0.007%[3]. The Mannesman certification for the beam tube shows a sulfur content of 0.001%. The effects of the low sulfur content are evident in metallographs of the welds, especially where the side clearance is a minimum. This produced a wide, flat weld with lower penetration. Studies[4] of autogenous welding of two different heats of stainless steel show that the weld will deviate

toward the low sulfur heat. This is graphically shown in Figure 14. Notice how the center of the weld is not immediately under the electrode, and, in fact, is 0.021 inch away from the axis of the electrode and toward the low-sulfur tube.

Solidification Cracking

The occurrence of a leak in the only weld made with the electrode located toward the 316LN tube required an investigation into the weld's potential for solidification cracking or "hot cracking."

Metal shrinks as a weld cools and begins to solidify, creating a strain within the weld. The strain is accommodated by movement of the liquid while the weld metal is mostly liquid. However, there may not be enough liquid to accommodate the strain as a greater percentage of the metal solidifies, causing cracks between the solid grains of metal in the weld. These cracks are called "solidification cracks." Solidification cracking becomes a problem for compositions with a large difference between the temperature at which solidification begins (the liquidus temperature) and the temperature at which solidification is complete (the solidus temperature). Also, metals which have a high linear coefficient of thermal expansion are more susceptible to solidification cracking. The linear coefficient of thermal expansion value is a measure of how much the metal shrinks as it cools.

Steel takes two primary forms: austenite and ferrite. Austenite is a face-centered-cubic crystal structure and has a high linear coefficient of thermal expansion. Ferrite is a body-centered-cubic crystal structure which has a lower linear coefficient of thermal expansion. Thus, austenitic stainless steels and other austenitic steels which usually contain large amounts of nickel, manganese, or nitrogen have a higher susceptibility to solidification cracking. In addition, all steels contain small amounts of sulfur, phosphorus, and other "tramp elements" that increase the difference between the liquidus temperature and the solidus temperature, thereby increasing the susceptibility to solidification cracking.

There are three primary modes for austenitic stainless steel solidification:

- solidify initially as austenite, and remain austenite down to room temperature or below;
- solidify initially as ferrite, then partially transform to austenite as it cools;
- solidify as a mixture of austenite and ferrite, with part of the ferrite transforming to austenite as it cools.

The determining factor for the mode of solidification is the alloy content and cooling rate.

Ferrite in small quantities is normally desirable in stainless steels welds because it reduces the overall linear coefficient of thermal expansion value, thus reducing the strain which contributes to solidification cracking. Ferrite also inhibits the formation of low melting-point compounds, especially FeP and FeS, thereby reducing the difference between the liquidus temperature and the solidus temperature.

Studies show the tendency toward solidification cracking can be controlled by careful control of the elements that produce a low-melting-point eutectic, such as phosphorous and sulfur.

Research[5] has found that susceptibility to solidification cracking is almost eliminated with a Chromium Equivalent/Nickel Equivalent ($[Cr/Ni]_{eq}$) ratio greater than 1.48, and is significantly affected when the sum of the weight percent of phosphorous and sulfur exceeds 0.01. Hence, ferrite-free alloys are produced with very strict controls on the impurity contents that promote solidification cracking. This is evident in electrode specifications where crack sensitive compositions can be available in a special grade with stricter limits on these elements.

In this study, the $[Cr/Ni]_{eq}$ for the weldment, calculated using different dilution ratios, ranged between 1.26 and 1.49, with an average of 1.37. This is shown in Figure 29. The sum of the weight percent of phosphorous and sulfur using the chemical certification values for the higher purity beam tube is 0.028 weight percent. The chemistry specified for AISI Type 304 alloy permits 0.030 weight percent maximum for sulfur and 0.045 weight percent maximum for phosphorous, for a combined 0.075 weight percent. Hence, the value for the weldment under study would be between 0.028 and 0.075 weight percent. Therefore, the impurity control is not possible for this situation for RHIC, but the $[Cr/Ni]_{eq}$ ratio greater than 1.48 may be applied.

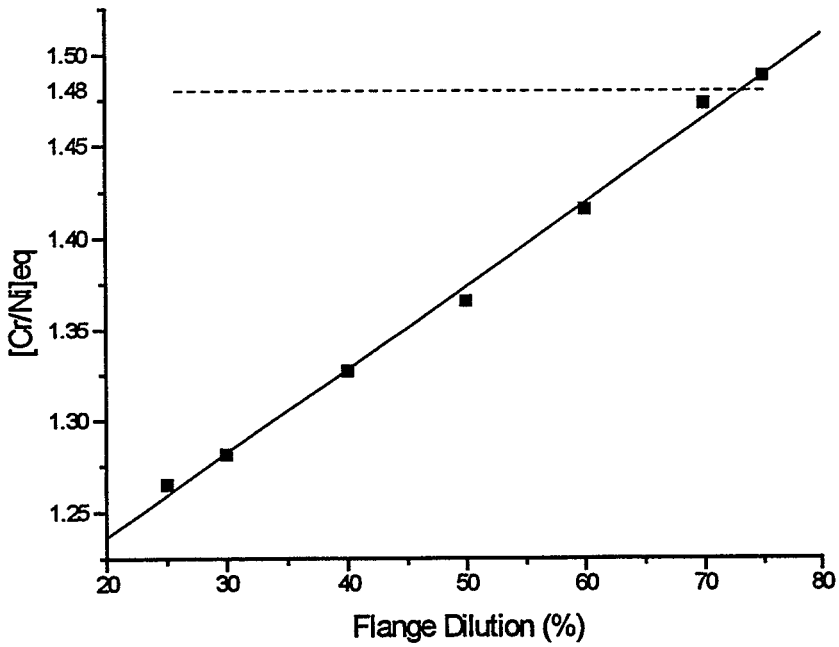

Figure 29 - Chromium/Nickel Equivalent Ratio for Various Weldment Dilution Rates (WRC-1992)

Weld Embrittlement

Generally, a higher ferrite content reduces the tendency for solidification cracking. An ideal ferrite range for welds other than those used in cryogenic service is a WRC Ferrite Number in the range of 5 to 10. While large amounts of ferrite reduce the likelihood of solidification cracking, ferrite can cause a weld to be susceptible to brittle fracture in-service. This brittle fracture problem occurs in two ways. Ferrite goes through a ductile-to-brittle transition as temperature decreases.

Also, a brittle material called sigma phase can form in the chromium rich areas where ferrite tends to form. Sigma phase generally requires long periods of time at relatively high temperatures to form, or repeated cycles at high temperature as in multi-pass welds, thus sigma phase is not a concern for RHIC except for multi-pass welds.

Ferrite also should be minimized for best toughness in cryogenic service. At cryogenic temperatures, ferrite reduces the Charpy V-notch absorbed energy and the fracture toughness of the 300-series stainless steels[6,7,8,9]. This is the reason why welding alloys for cryogenic service are either ferrite-free or very low ferrite. Therefore, the commercial manufacturing practice to assure just enough ferrite in the weld to prevent solidification cracking is not acceptable because it contradicts the superaustenitic material necessary to meet the high fracture toughness requirements[10] defined for the severe 4 K cryogenic temperatures at which RHIC must operate.

Constitution Diagrams

During the 1940's, Anton Schaeffler and other researchers[11] observed a direct correlation between the amount of ferrite left in a weld deposit after it cooled and the susceptibility of the weld metal to solidification cracking. Schaeffler devised a diagram, based upon a large amount of data that he collected from numerous sources, which would predict the percent of ferrite left in a stainless steel weld after it cooled. The Schaeffler Diagram does not take into consideration the nitrogen content of the weld metal.

William DeLong observed that a region of the Schaeffler Diagram, where most of the stainless steels were plotted, could be made to predict ferrite more accurately with some changes to the formulas.[12] He published the DeLong Diagram in 1973, incorporating the effect of nitrogen which had been overlooked in the Schaeffler Diagram. The DeLong diagram is a finely-tuned subset of the Schaeffler range, designed specifically for the 300-series stainless steel welds containing small amounts of ferrite. Earlier versions of the DeLong Diagram represented ferrite in units of volume percent only. A later version was developed after the Welding Research Council Subcommittee on the Welding of Stainless Steels promulgated a standard using the term Ferrite Number to define the ferrite content by its magnetic response. Ferrite Number (FN) and volume percent ferrite designations are very close at low ferrite content and begin to diverge at ferrite contents near 8. FN values were originally thought useful for predicting weld metal susceptibility to solidification cracking. However, recent studies[13,14,15] have emphasized that the solidification mode is more accurate than FN for predicting the resistance to solidification cracking.

Inaccuracies in both the DeLong and Schaeffler diagrams have become evident with the generation of new alloys and data. Cryogenic applications require the most stringent ferrite controls and justify the most accurate solidification mode prediction.[16] The Welding Research Council Subcommittee on the Welding of Stainless Steels developed and refined a new constitution diagram. The original diagram, WRC-1988, was published in 1988.[16] The refined diagram, WRC-1992,[17] includes a factor for copper in the nickel equivalent. The WRC Diagram differs from its predecessors in several important respects. Manganese is deleted from the equation for the "Nickel Equivalent" that forms the vertical axis of the diagram, and silicon is deleted from the equation for the "Chromium Equivalent" that forms the horizontal axis of the diagram. The coefficients for

carbon and nitrogen in the "Nickel Equivalent" are no longer equal, and the coefficient for niobium (columbium) is increased. The new diagram presents iso-ferrite lines from 0 FN to 100 FN (100 FN being roughly equivalent to 65 volume percent ferrite), covering a much broader range than the DeLong Diagram. Finally, the new diagram separates compositions according to their solidification mode with boundaries for fully austenitic (A), primarily austenitic with some eutectic ferrite (AF), primarily ferritic with some eutectic austenite (FA), or fully ferritic (F). The use of the WRC-1992 Diagram increases the prediction accuracy when the level of copper becomes significant; about 0.5%.

Prediction Accuracy

The accuracy of this new diagram in predicting measured Ferrite Numbers has been independently compared with the accuracy of the DeLong Diagram by the International Institute of Welding, Subcommission II-C (IIW Document II-C 834-88). The predictions of the new diagram, for over two hundred compositions independent of the database of the diagram, were within ±2.5 FN of the measured values in over 70% of the cases, versus about 45% of the cases when the DeLong Diagram was used for prediction. A scarcity of data at relatively high concentration levels for some elements suggest restrictions for the use of the new diagram. When manganese is less than 10% by weight and nitrogen is less than 0.2% by weight, the new diagram has an 88% chance of predicting the FN with an accuracy of ±2.5 FN when compared to the 68% chance for the DeLong diagram.

The predicted ferrite content is approximate; the ferrite content of a weld will depend upon the actual composition values, the heat input, and other welding parameters. The accuracy also is affected by the Schaeffler, DeLong, and WRC-1988 Constitution diagram accuracies as reported in the literature and by the accuracy of chemical analysis used in making the calculations. Ferrite predictions were made using a computer program from the American Welding Institute called FERRITEPREDICTOR. While the program has provisions for calculating and plotting Ferrite Number using the Schaeffler, DeLong, and WRC-1988 Constitution Diagrams, we choose the WRC-1992 Constitution Diagram because of its greater accuracy.

Sample Ferrite Numbers

The chemical compositions used for the Ferrite Number calculations were the beam tube product analysis certification from Mannesman and the nominal composition for AISI Type 304 stainless steel for the flanges. The FERRITEPREDICTOR program considers a variable dilution ratio between the different base metals for an autogenous weldment, but there are no rules for determining the dilution ratio. FERRITEPREDICTOR was used to calculate and plot the Ferrite Number for various dilution ratios between 75% beam tube/25% flange and 25% beam tube/75% flange. Ferrite numbers ranged from -0.1 to 3.4, shown in Figure 30. Individual FERRITEPREDICTOR WRC-1992 constitution diagrams showing the predicted Ferrite Number for the flange, beam tube, and the weldment for the given dilution ratio were generated. A composite constitution diagram also was produced, and is shown in Figure 31. The Figure shows the predicted Ferrite Number for the flange and the beam tube, represented by a box symbol, and the predicted Ferrite Numbers for the weld metal for dilution ratios of 75%/25%, 70%/30%,

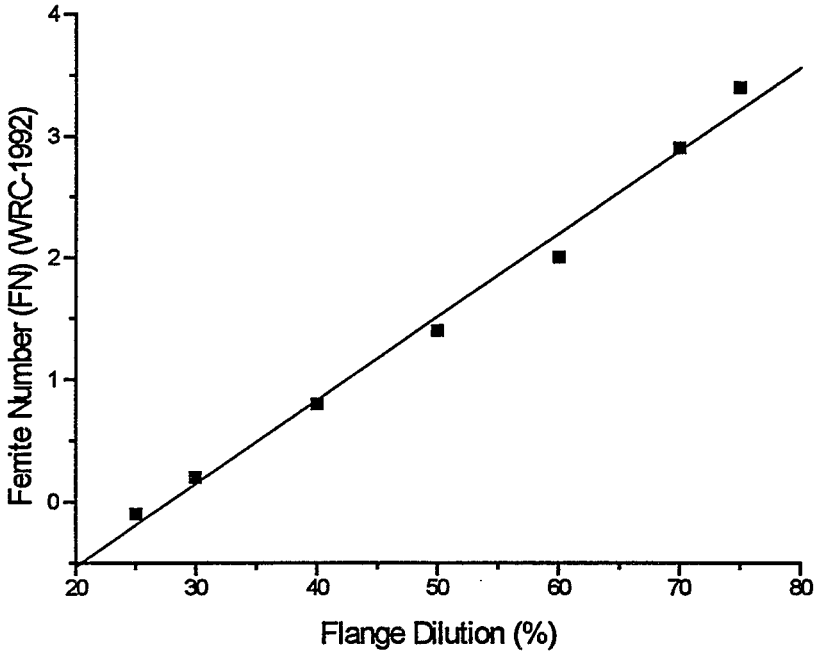

Figure 30 - Ferrite Number Prediction for Various Weldment Dilution Ratios (WRC-1992)

60%/40%, 50%/50%, 40%/60%, 30%/70%, and 25%/75%, percent flange dilution versus percent beam tube dilution, represented by cross symbols. A predicted Ferrite Number of zero or less for the weldment would mean the weldment solidification mode was completely austenitic. We believe this completely austenitic solidification mode is the cause of the solidification cracking observed in weld specimen #9B. In addition, our testing showed the difference between a weld that leaked and a weld with satisfactory penetration was an electrode location variation of just 0.026 inch, making this particular autogenous weld unsuitable for a manual weld.

These diagrams only predict ferrite content based upon the weld metal composition. There are other factors that effect ferrite in the weld metal. One such factor is the primary phase in which the material solidifies; in this case it is primary austenite. Another factor is the cooling rate of the weld which is solely dependent upon the weld procedure and process. When producing autogenous welds a loss in ferrite occurs unlike welds made with filler metal where the loss in ferrite is corrected by the addition of filler metal. On multi-pass welds a loss of ferrite takes place in the heat affected zone, resulting in a loss of ductility and rendering the weld susceptible to fissuring under strain.[18] Therefore, welds that were repaired using filler metal should perform satisfactorily. However, multi-pass autogenous welds may have been compromised. The most severe stresses to which these welds will be subjected are from temperature extremes. Hence, welds which have been cold-shocked with a cryogen and subsequently passed a vacuum leak check also should perform satisfactorily in service.

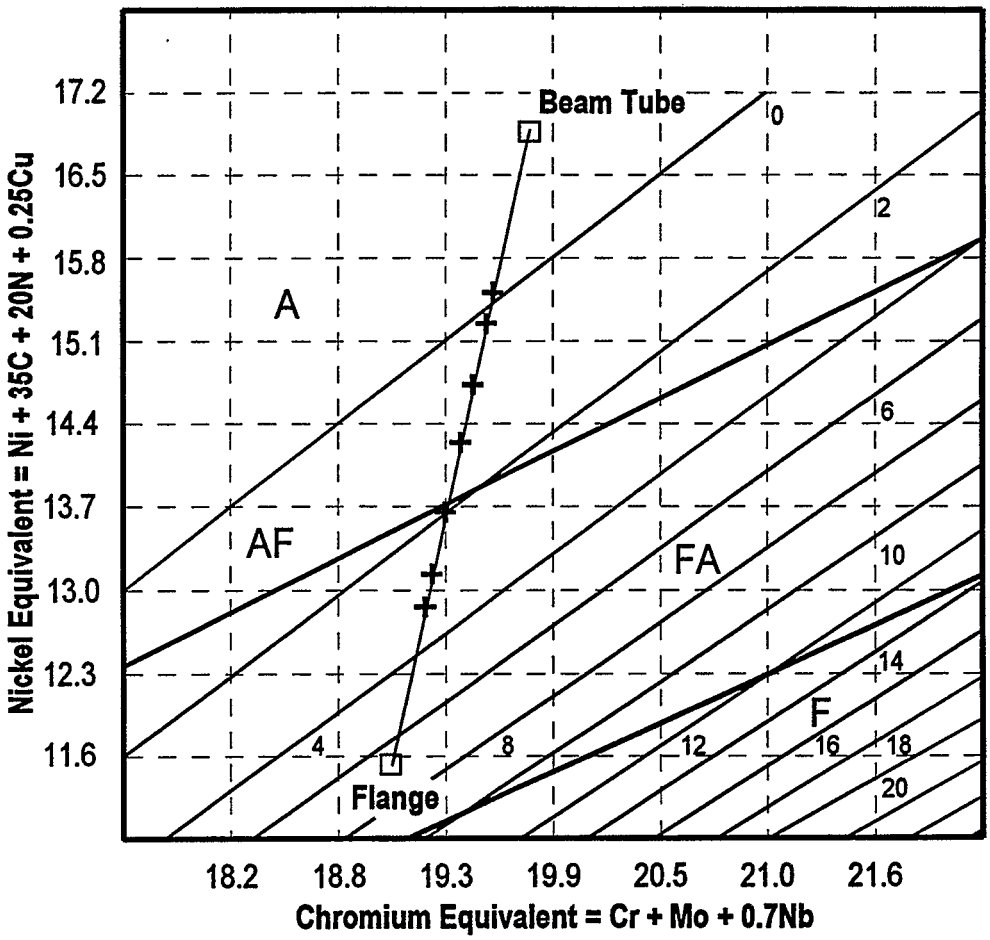

Figure 31 - WRC-1992 Constitution Diagram for Beam Tube-to-Flange Weld Metal

Weld Procedures

This study validated an automatic weld procedure with very specific parameters. Deviation from these parameters will have unknown results. The sample welds used tubes with ovality no greater than 0.002 inch. Greater variation than this will cause greater variation in electrode gap, which is a significant parameter. It is believed that ovality affects the performance of the Wachs cutter used to cut the tube. Therefore the tube ovality must be corrected for proper welding. Manufacturers of tube welders recommend the tube be cut square with the tube axis as close to zero degrees as possible, and the tube end should be faced. This is to prevent gaps in the fit-up of the joint, and any gaps should be less than five percent of the wall thickness. Also, the tube inside and outside diameter must be burr-free with no chamfer. These conditions also will significantly affect penetration and weld composition. Using a Wachs cutter will assure a proper tube end preparation for this weld. The flanges shall be tack welded to the tube in at least three places to assure gap-free fit-up during the weld process. This shall be accomplished with the tube butting against the flange shoulder. This is not possible with too generous a radius in the flange counterbore without a chamfer on the tube outer diameter. The tube is too thin for a consistent chamfer depth that will not affect penetration, therefore the flange counterbore corner should be undercut to eliminate interference with the outer diameter of the tube.

Conclusions

The beam tube-to-flange weld can be performed automatically. All automatic welds achieved the minimum required penetration of 0.025 inch. However, in combination with a shield gas with 5% hydrogen, this automatic weld will assure the deepest and most consistent weld penetration with 21% less heat input than the welds using 100% argon. In this investigation we have found that the addition of hydrogen produce 14% greater penetration, all other parameters being equal.

The welds produced with hydrogen additions were exceptionally oxidation-free, with little or no cleaning required. This contrasts with the high heat, 100% argon welds which required wire brushing to remove the oxidation.

The low sulfur content of the beam tube causes the weld to be displaced toward the tube. This can be corrected by electrode location.

Electrode location is also critical to weld metal composition and solidification mode. Varying the electrode location by just 0.026 inch will result in solidification cracks and a leaking weld. This factor makes this weld unsuitable to manual welding.

When producing autogenous welds a loss in ferrite occurs unlike welds made with filler metal where the loss in ferrite is corrected by the addition of filler metal. Welds that were repaired using filler metal should perform satisfactorily. Any leaks which occur shall be repaired using filler metal.

Multi-pass autogenous welds may have been compromised. Welds which have been cold-shocked with a cryogen and subsequently passed a vacuum leak check should perform satisfactorily in service. Any multi-pass welds which are found to leak after cold-shock shall be repaired by cutting off the flange and rewelding with a new flange and an automatic process.

Reliable penetration and leak-free welds are not possible for this joint unless automatically welded.

Precise fit of the beam tube to the flange must be maintained within manufacturing tolerances. Deviation from the parameters developed in this evaluation will have unknown results. Ovality shall be no greater than 0.002 inch. Using a Wachs cutter will assure a proper tube end preparation for this weld, specifically;

- the tube shall be cut square with the tube axis as close to zero degrees as possible
- the tube end should be faced to prevent gaps in the fit-up of the joint
- the tube inside and outside diameter must be burr-free with no chamfer.

The flanges shall be tack welded to the tube in at least three places to assure gap-free fit-up during the weld process. The flange counterbore corner shall be undercut to eliminate interference with the outer diameter of the tube.

[1] L.P. Connor, Ed., *Welding Handbook: Volume 1, Welding Technology*, Eight Edition, 1987
[2] G. E. Linnert, *Welding Metallurgy: Carbon and Alloy Steels, Vol. 1 Fundamentals*; Fourth Edition, 1994
[3] P. Burgardt and C.R. Heiple; *Interaction Between Impurities and Welding Variables in Determining GTA Weld Shape*, Welding Journal 65(6), June 1986: p. 150s
[4] J.L. Fihey and R. Simoneau; *Weld Penetration Variation in GTA Welding of Some 304L Stainless Steels*, American Welding Society Conference, Kansas City, Missouri, May 16-19, 1982
[5] V.Kujanpaa, N. Suutala, T. Takalo, and T. Moisio; Welding Research International, 9(2): 55, 1979
[6] T.A. Siewert, *How to Predict Impact Energy from Stainless Steel Composition*, WD&F 51, 1978: pp. 88-90
[7] E.R. Szumachowski, H.F. Reid, *Cryogenic Toughness of SMA Austenitic Stainless Steel Weld Metals: Part I — Role of Ferrite*, Welding Journal 57(11), 1978: pp. 325s - 333s
[8] D.T. Read, H.I. McHenry, P.A. Steinmeyer, R.D. Thomas, Jr., *Metallurgical Factors Affecting the Toughness of 316L SMA Weldments at Cryogenic Temperatures*, Welding Journal 59(4), 1980: pp. 104s - 113s
[9] T.A. Siewert, *Predicting the Toughness of SMA Austenitic Stainless Steel Welds at 77 K*, Welding Journal 65(3), 1986: pp. 23 - 28
[10] S. Kane, *Fracture Toughness Requirements for RHIC Cryogenic Design;* RHIC Project Tech Note AD/RHIC/RD-40, May 1992
[11] A.L. Schaeffler, *Constitution Diagram for Stainless Steel Weld Metal; Metal Progress*, 56 (11), 1949: pp. 680-680B
[12] W.T. DeLong, *Ferrite and Austenitic Stainless Steel Weld Metal*; Welding Journal, 53 (8), 1974: pp. 273s-286s
[13] N. Suutala, *Effect of Manganese and Nitrogen on the Solidification Mode in Austenitic Stainless Steel Welds*; Met. Trans. A, 1982
[14] J.C. Lippold, W.F. Savage, *Solidification of Austenitic Stainless Steel Weldments: Part III — the Effect of Solidification Behavior on Hot Cracking Susceptibility*; Welding Journal 61(12), 1982: pp. 388s - 396s
[15] V. Kujanpaa, *Role of Steel Type and Impurities in Solidification Cracking in Austenitic Stainless Steel Welds*, Metal Construction, 1985: pp. 23-25
[16] T.A. Siewert, C.N. McCowan, D.L. Olson, *Ferrite Number Prediction to 100 FN*; Welding Journal, Dec. 1988: p. 289s
[17] D.J. Kotecki, T.A. Siewert, *WRC-1992 Constitution Diagram for Stainless Steel Weld Metals: A Modification of the WRC-1988 Diagram*; Welding Journal, May 1992: p. 171s
[18] S. Kou, *Welding Metallurgy*, John Wiley & Sons, 1987, pp. 187

APPENDIX A

Worksheets
for
Welding Sample Parameters

SAMPLE # 1 FLANGE I.D. 2.896 TUBE OVALITY .002"

GAS 95Ar/5H

WELD SCHED. 1

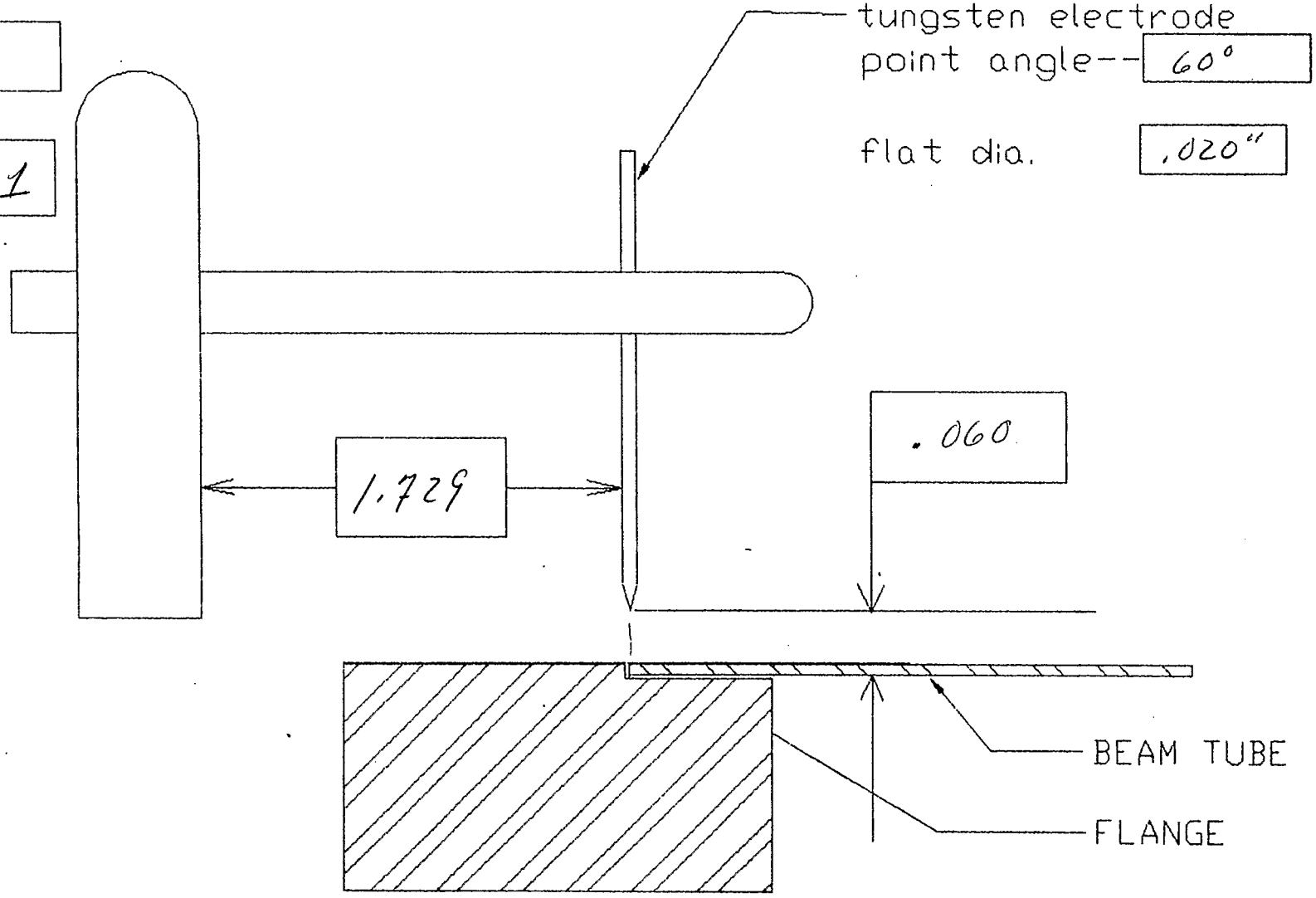

SAMPLE # 2 FLANGE I.D. 2.898 TUBE OVALITY .001

GAS 95 AR/5 H

WELD SCHED. 2

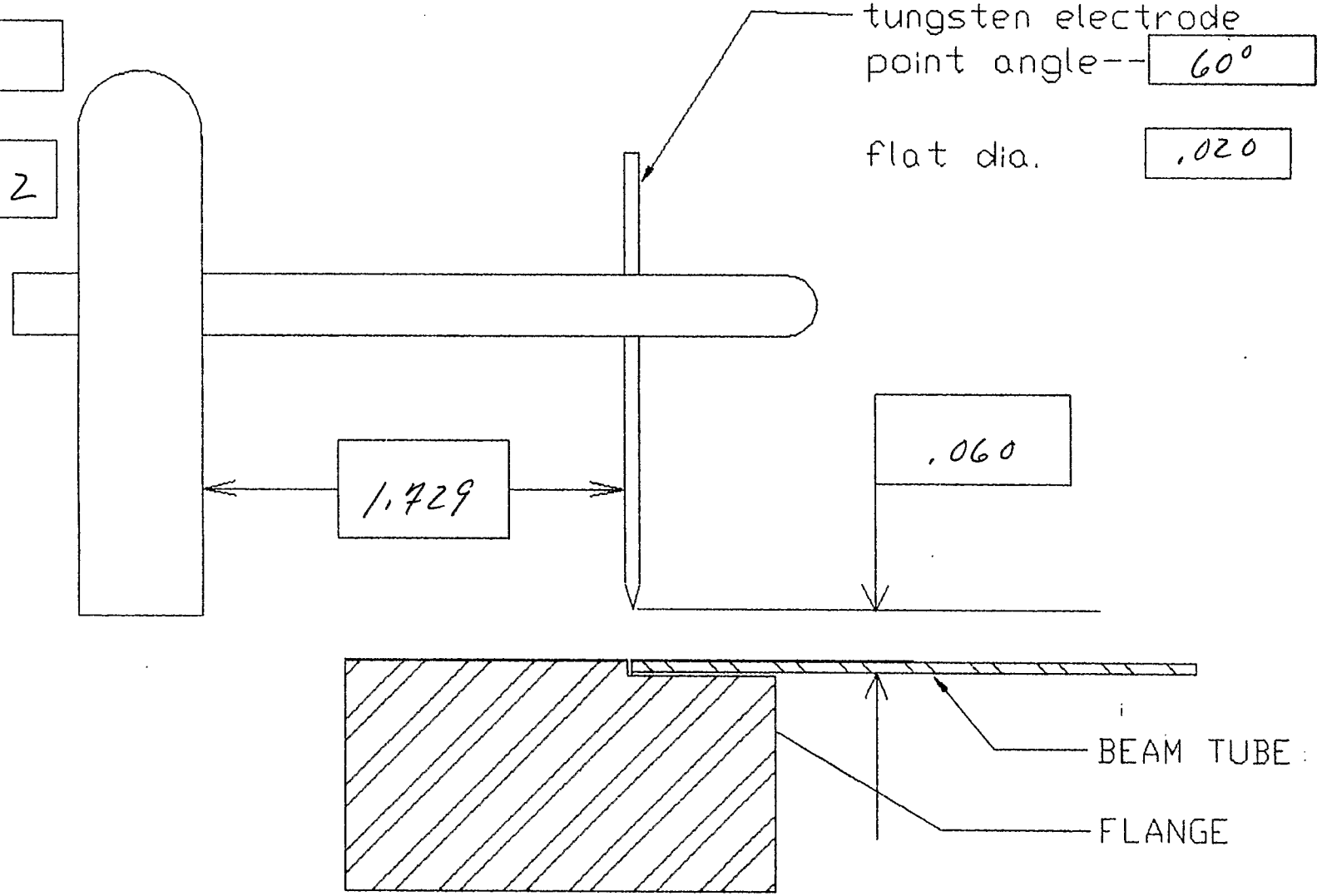

SAMPLE # 3 FLANGE I.D. 2.894 TUBE OVALITY .001"

GAS 95Ar/5H

WELD SCHED. 3

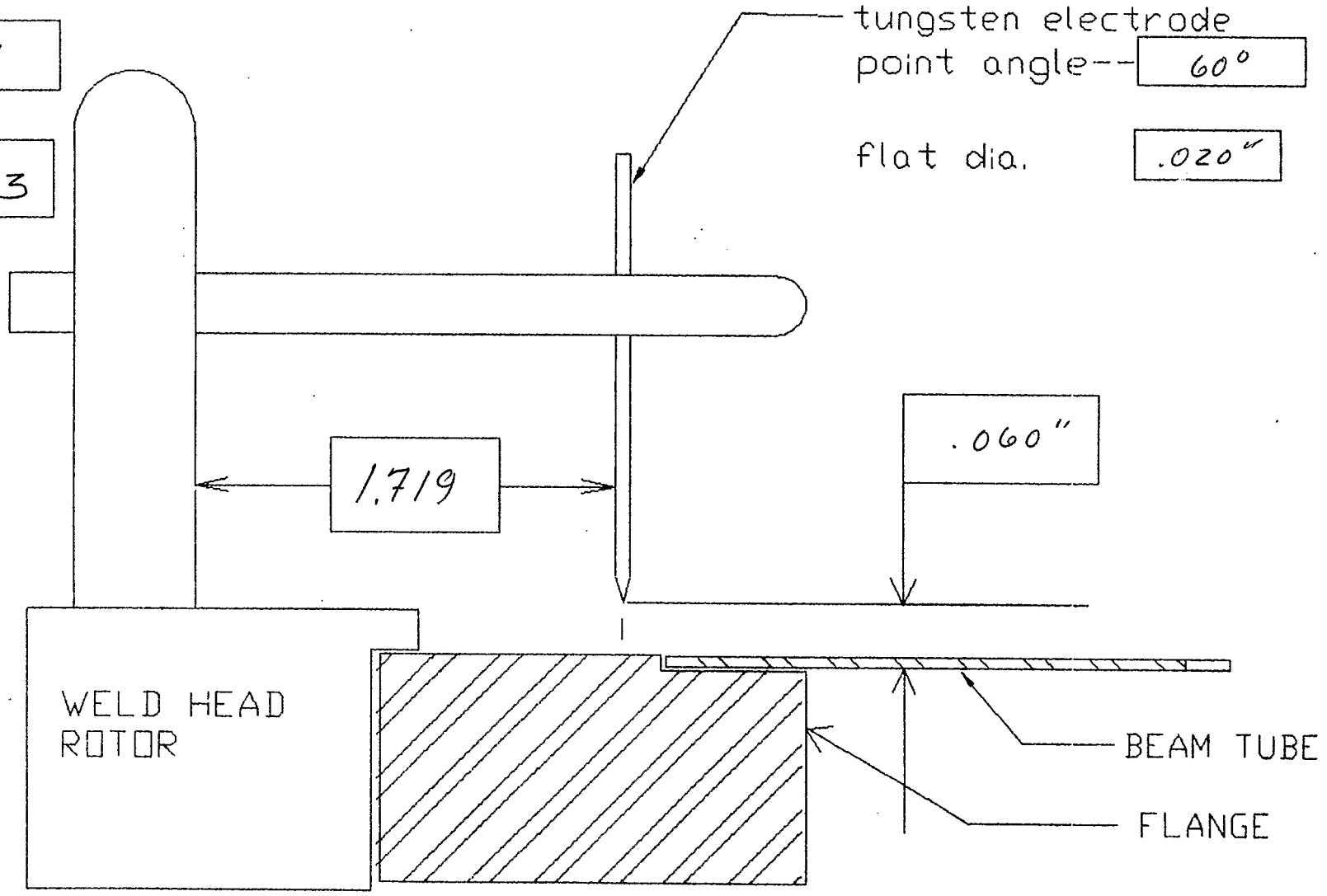

SAMPLE # 4 FLANGE I.D. 2.896 TUBE OVALITY .001

GAS 95 Ar/5 H

WELD SCHED. 1

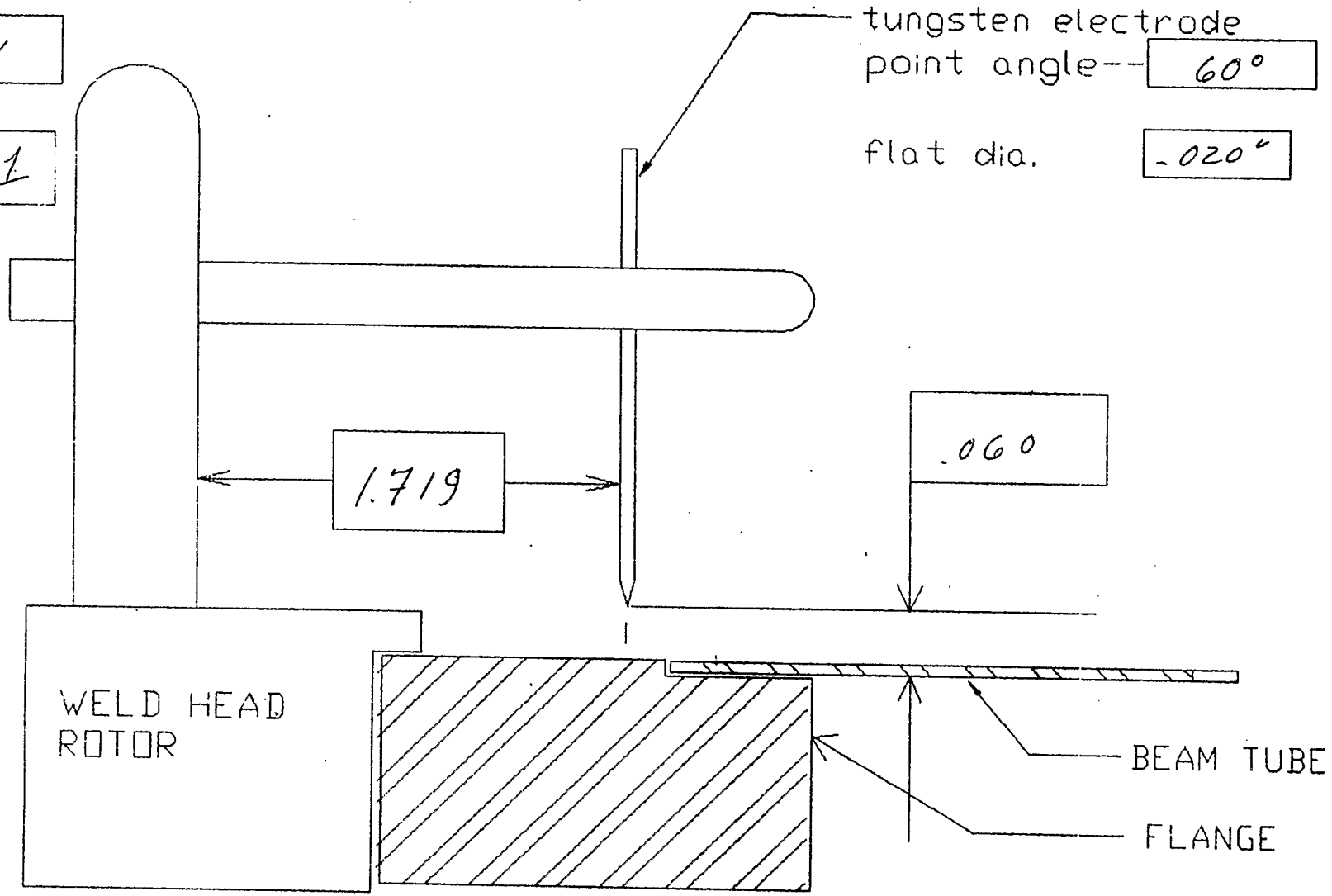

SAMPLE # 5 FLANGE I.D. 2.895 TUBE OVALITY —

GAS 95 Ar / 5 H

WELD SCHED. 2

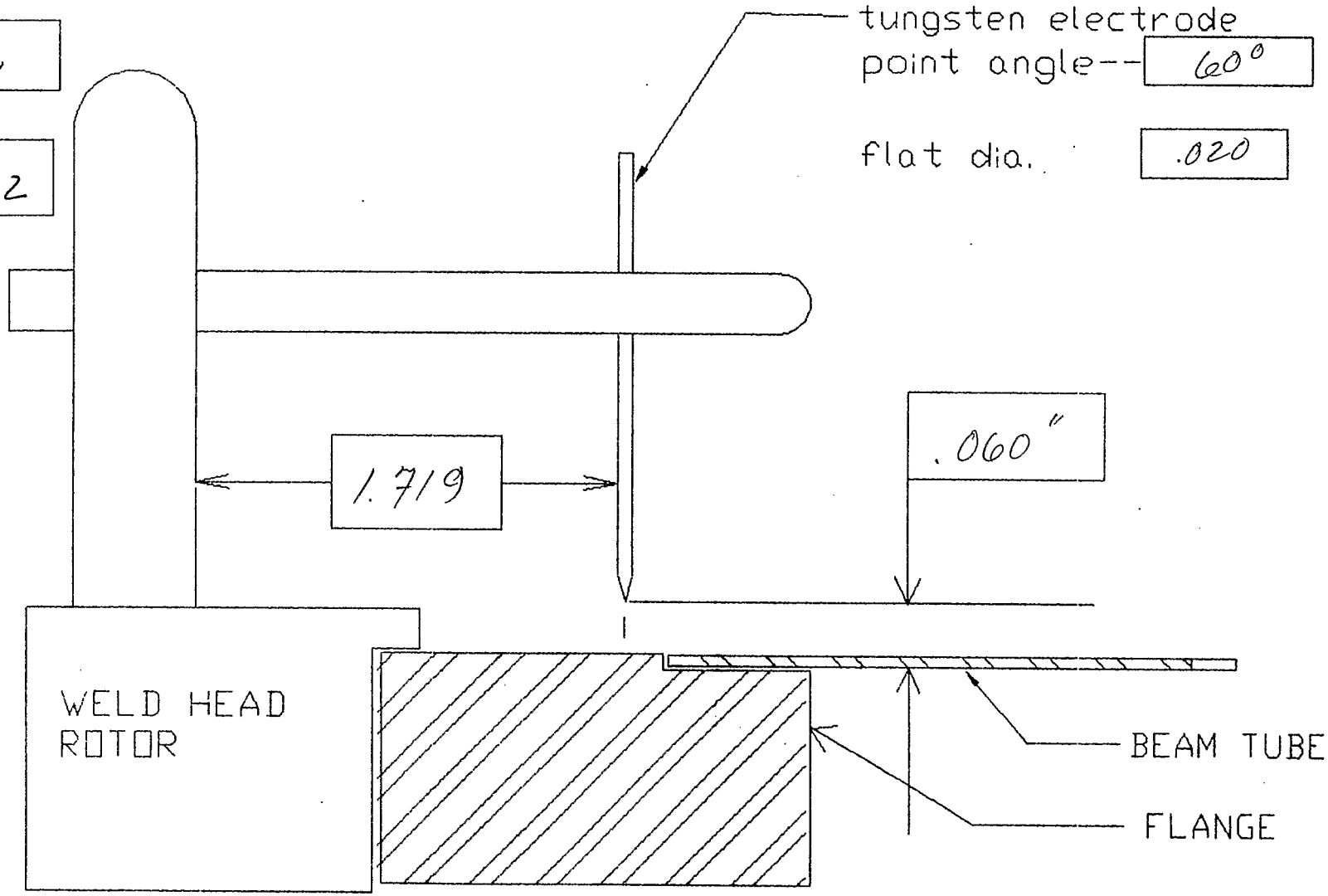

SAMPLE # 6 FLANGE I.D. 2.896 TUBE OVALITY —

GAS 100 Ar

WELD SCHED. 2

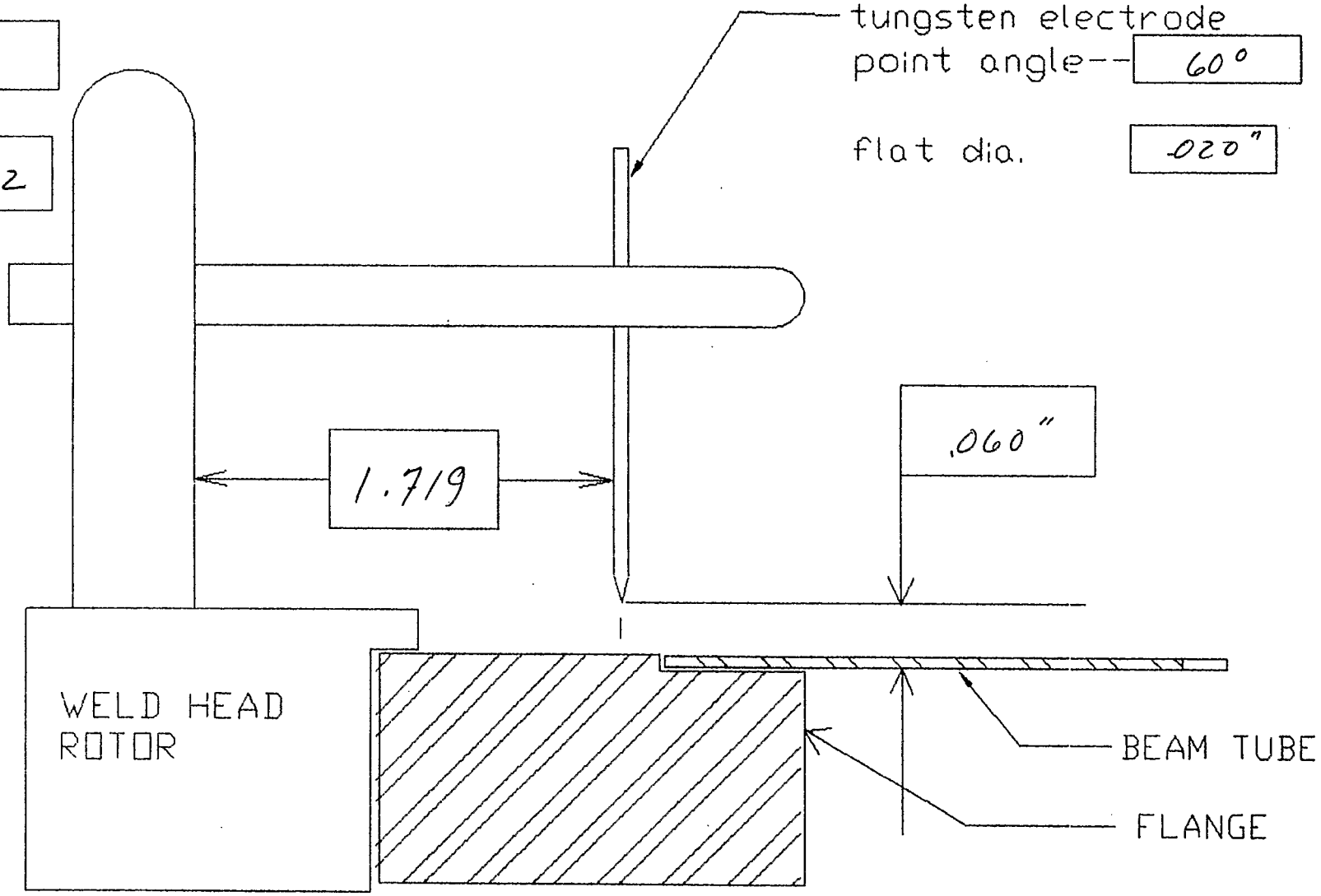

SAMPLE # 7 FLANGE I.D. 2.896 TUBE OVALITY .001

GAS 100% Ar

WELD SCHED. 3

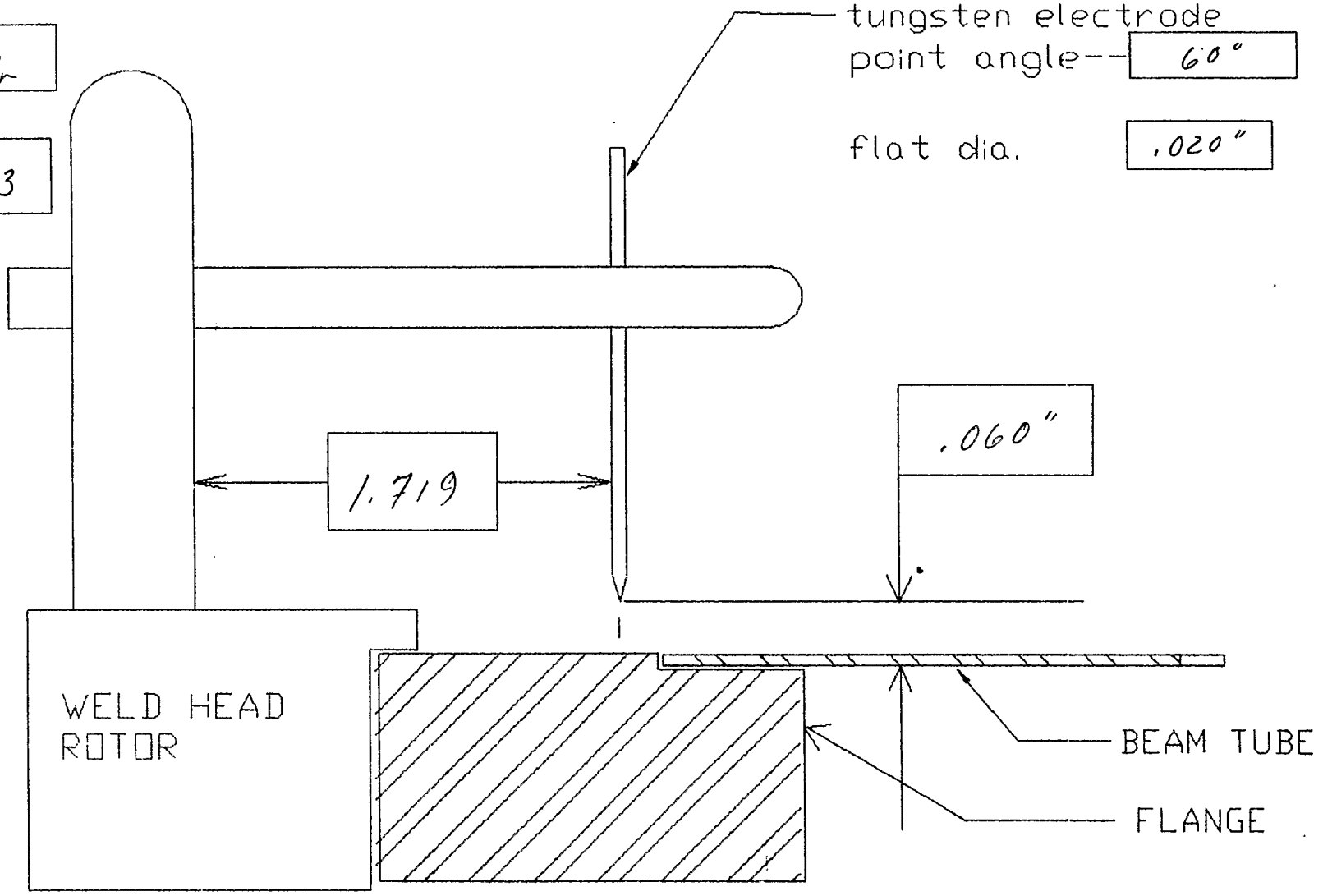

SAMPLE # 8 FLANGE I.D. 2896 TUBE OVALITY .001

GAS 100 Ar.

WELD SCHED. 4

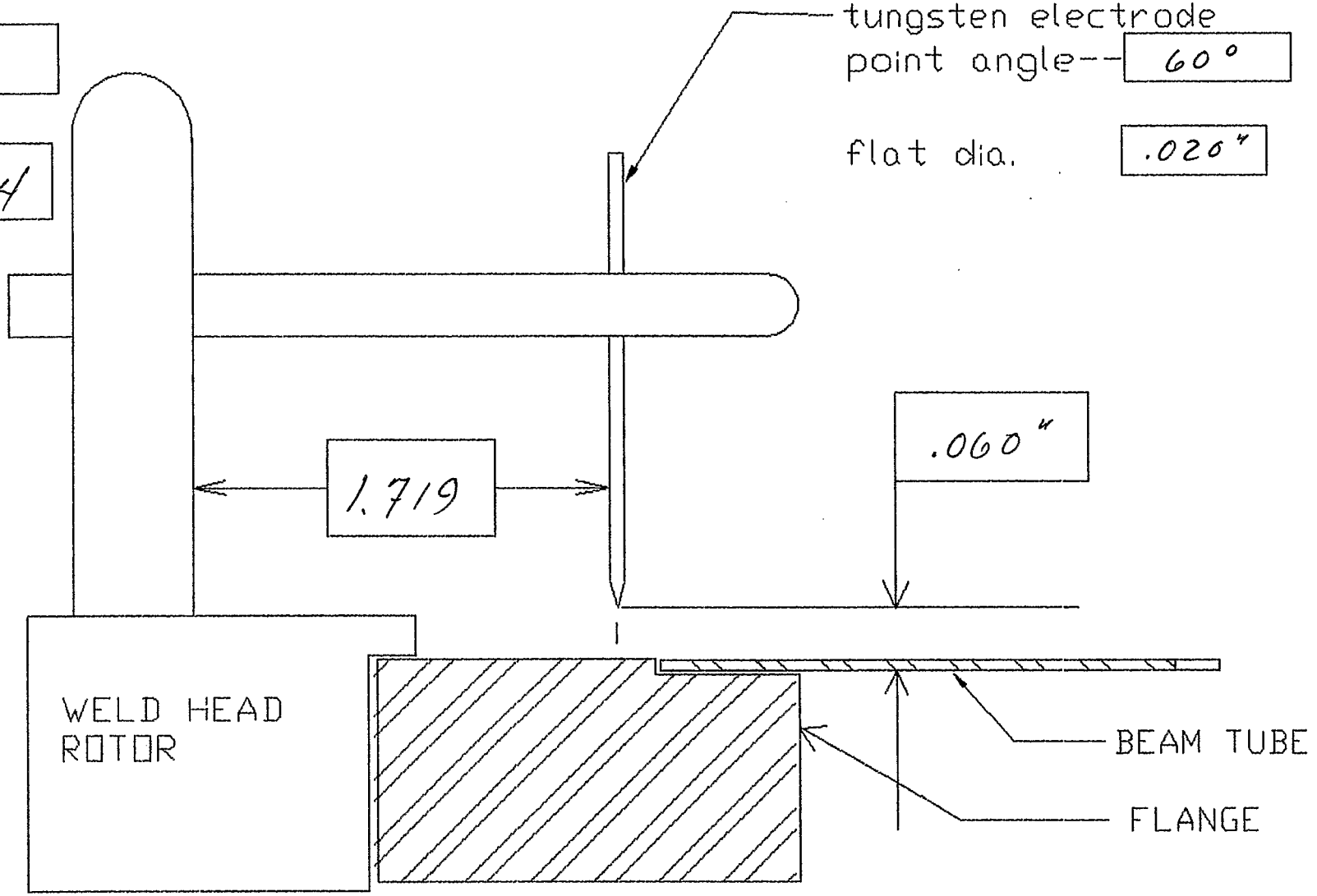

SAMPLE # 9 FLANGE I.D. 2.895 TUBE OVALITY .001"

GAS 100% Ar

WELD SCHED. 4

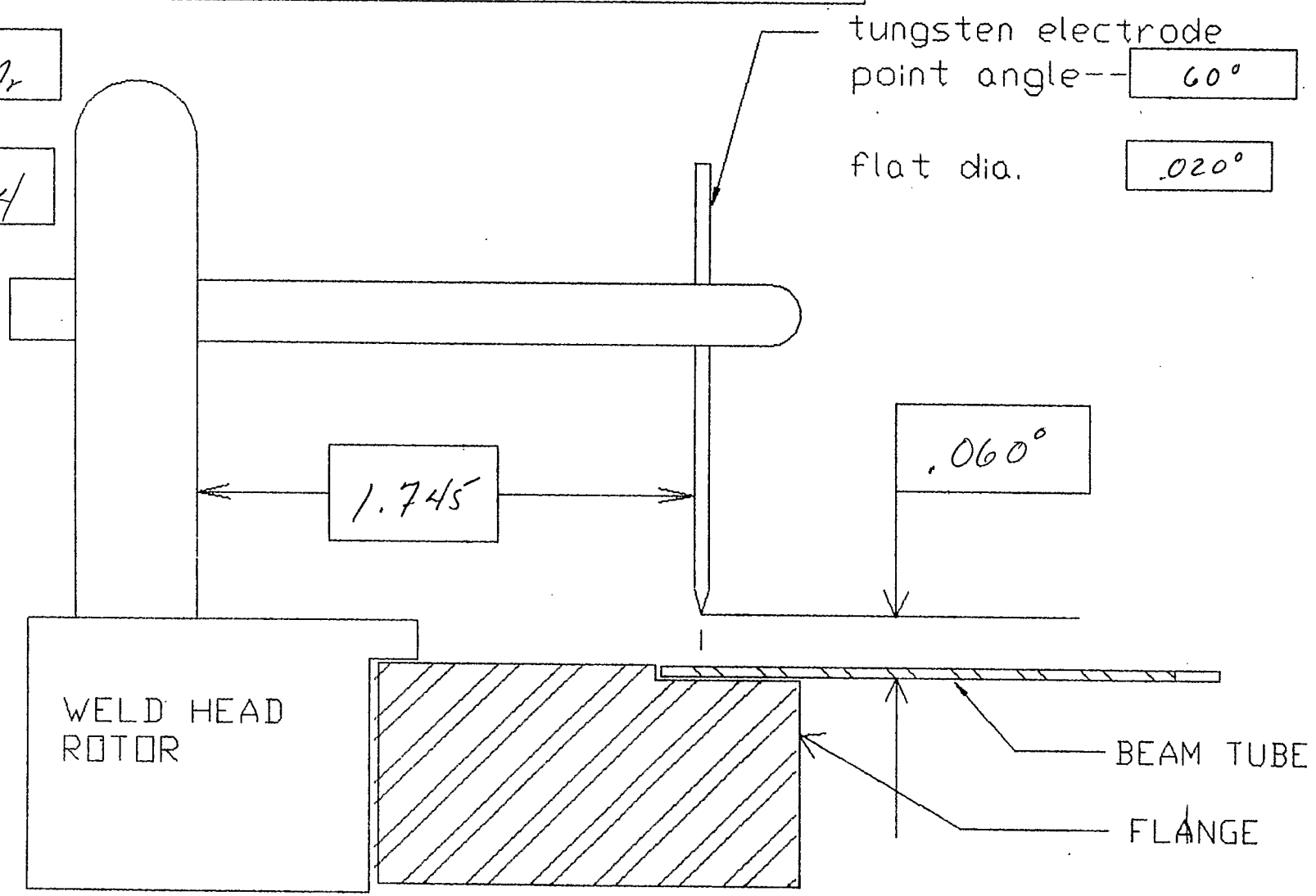

SAMPLE # 10 FLANGE I.D. 2.896 TUBE OVALITY .~~007~~

GAS 100% Ar.

WELD SCHED. 5

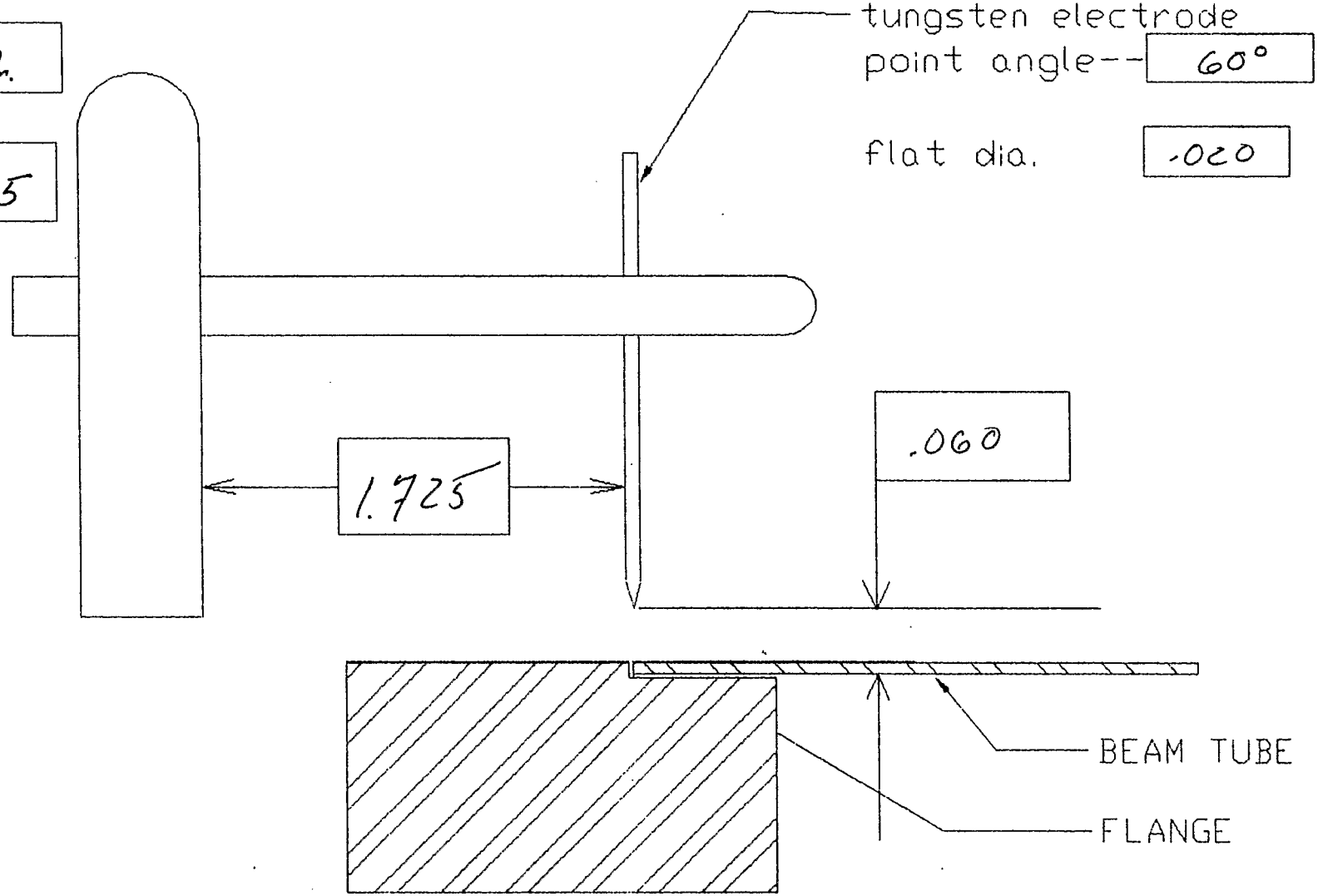

SAMPLE # 11 FLANGE I.D. TUBE OVALITY

GAS 95/5

WELD SCHED. 2

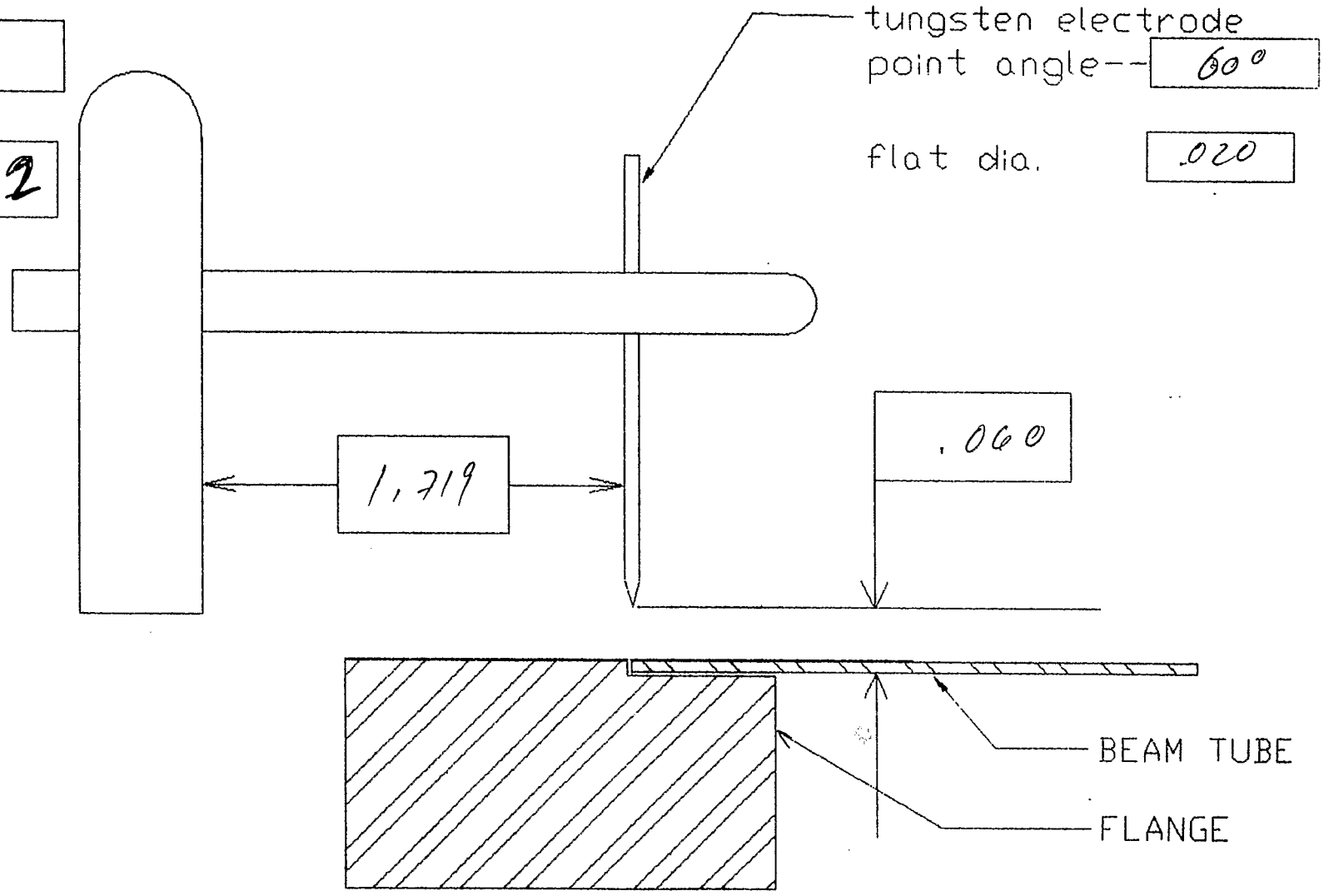

SAMPLE # 12 FLANGE I.D. TUBE OVALITY

GAS 95/5

WELD SCHED 3